The Pennsylvania State University

The Graduate School

Department of Electrical and Computer Engineering

PERFORMANCE ANALYSIS OF THE LAMP RAYLEIGH/RAMAN LIDAR SYSTEM

A Thesis in

Electrical Engineering

by

Paul A.T. Haris

Submitted in Partial Fulfillment of the
Requirements for the
Degree of

Master of Science

December 1992

We approve the thesis of Paul A. T. Haris.

Date of Signature

Charles R. Philbrick
Professor of Electrical Engineering
Thesis Advisor

John D. Mathews
Professor of Electrical Engineering

Chih-Chung Yang
Associate Professor of Electrical . Engineering

Larry C. Burton
Professor of Electrical and Computer Engineering
Head of the Department of Electrical and Computer. Engineering

_____

Paul A.T. Haris

ABSTRACT

A performance analysis of a two color Rayleigh/Raman lidar system, LAMP (Laser Atmospheric Measurement Program), has been characterized and will be presented. LAMP was constructed at The Pennsylvania State University during the summer of 1991, and was developed to measure temperature and density from the ground to 80 km, and to measure the concentrations of nitrogen (N_2) and water vapor (H_2O) from the ground to 35 km and 5 km, respectively. Expected photon returns from the several channels of the LAMP system were calculated using the lidar equation. Each term of the lidar equation has been critically analyzed for its effect on the transmitted and returning signal. The transmission and number density of the atmosphere were simulated using the LOWTRAN 7 and U.S. Standard Atmosphere, 1976 models. Optical efficiencies for the near and far fields of the LAMP receiver, a classical Cassegrain telescope, have been calculated using a computer simulated model. Optical efficiencies for the transmitter, receiver, and detector have also been measured. Data from the LADIMAS (LAtitudinal Distribution of Middle Atmospheric Structure) campaign, measured between September 1991 and January 1992, are presented to support the performance analysis and to describe the photon losses in the troposphere and lower stratosphere. The performance analysis serves as a first order approximation to the LAMP operating characteristics, and shows the areas where emphasis must be placed to develop a more useful model and an improved instrument.

TABLE OF CONTENTS

LIST OF FIGURES

LIST OF TABLES

ACKNOWLEDGMENTS

I would like to thank my advisor, C. R. Philbrick, for providing me with once-in-a-lifetime experiences. His support and guidance have been invaluable throughout all of my learning endeavors. Support by my committee members, J. D. Mathews and C. C. Yang, is also gratefully appreciated.

I would like to thank Dan Lysak, Tim Stevens, Subha Maravada, Yi-Chung Rau, Dave Machuga, George Evanisko, Steve McKinley, Tom Petach, and Glen Pancoast for their contributions to this thesis.

Thanks are due to the Applied Research Laboratory, the U.S. Air Force, and the Aerospace Education Foundation for their support of my graduate schooling.

The effort to prepare the LAMP instrument has been supported by the National Science Foundation, the U.S. Navy's Environmental Systems Program Office, and The Pennsylvania State University's Applied Research Laboratory and College of Engineering. The campaign was made possible by an invitation from the Alfred-Wagner-Institute to participate in the RV POLARSTERN voyage. Appreciation to several colleagues, particularly U. von Zahn and D. Offermann, is gratefully acknowledged.

Chapter 1

INTRODUCTION

In the presence of a changing environment and a modern society, the need for monitoring the Earth's atmosphere has steadily increased. Advances in remote sensing instrumentation have provided the opportunity to obtain accurate measurements of atmospheric composition, structure, and dynamics without the complexity of balloon and rocket-borne instruments. Leading these instruments is lidar (LIght Detection and Ranging). Lidar is similar to radar, using visible light instead of microwaves. Lidar's history began in 1956 when Elterman set up a search light and a telescope in a bistatic configuration to measure atmospheric density [2]. The receiver telescope scanned the search light beam to provide range resolution. These pioneering measurements were later improved with the development of the theory of the optical laser by Schawlow and Townes [20], and the construction of the first laser in 1960 by Theodore H. Maiman [8]. The laser provided high intensity light, in a collimated beam, which allowed for the signal-to-noise ratio of the detected signal to be increased by narrowing the field of view of the receiving system. The greatest advance to laser technology and lidar measurements came with the development of the Q-switch by McClung and Hellwarth in 1962 [9]. The Q-switch produced high powered laser energy in short pulses, making high range resolution possible in a monostatic configuration. Laser pulses, of spatial length shorter than the range resolution desired, are sent into the atmosphere and scattered by molecules and particles. The light scattered in the direction of the receiving system is collected and

processed to reveal specific information on atmospheric properties, such as, density and temperature. Range is calculated by measuring the elapsed time from laser firing to data collection.

The scope of lidar measurement techniques is vast and steadily increasing. Measurements of diurnal and seasonal temperature variations have been made in the middle atmosphere [1,18] and lower thermosphere [11,26] using Rayleigh and resonance fluorescence lidar techniques, respectively. Environmental effects caused by recent major volcanic eruptions, such as, El. Chichon in 1982 and Mt. Pinatubo in 1991, have increased the interest in monitoring the stratospheric aerosol layer [5,22,23]. Temporary changes in mean temperatures, depletions in ozone [3], and increases in pollutants have also shown the need of monitoring trace constituents in the troposphere and stratosphere.

This thesis will present a performance analysis of the LAMP lidar. To do this, the terms of the lidar equation, which predict the expected number of photons to be collected by the system, will be critically analyzed. A model will be designed to include the operating characteristics of the system in order to produce an expected photon return profile. This profile will be compared to measured data, and any deviations will be discussed. The comparison will target areas in the model and system that need improvement. A quick overview of the LAMP design and testing, and the LAMP instrument will be presented here, while the analysis and results of the LAMP performance will be presented in subsequent chapters.

1.1 LAMP Design and Testing

In the summer of 1991, The Pennsylvania State University's LAMP (Laser Atmospheric Measurement Program) lidar was completed and tested in preparation for the LADIMAS (LAtitudinal Distribution of Middle Atmospheric Structure) campaign which took place between September 1991 and January 1992 [15]. The goal of the LADIMAS campaign was to latitudinally measure atmospheric dynamics, density, temperature, and trace constituents from the ground to 120 km. The LAMP lidar measures density and temperature from the ground to 80 km and concentrations of nitrogen and water vapor from the ground to 35 km and 5 km, respectively [21]. It was deployed to Norway for the first leg of the campaign, where it took correlative measurements with meteorological rockets [15]. With a resupply stop in Germany, the LAMP lidar was placed aboard the German research vessel RV Polarstern where it was to make the majority of its measurements for the campaign. The RV Polarstern sailed from Norway to Antarctica on its yearly resupply voyage to Antarctic bases. Selected data from the LADIMAS campaign will be presented to show the effects of atmospheric conditions on lidar measurements.

1.2 LAMP Instrument

The Penn State LAMP lidar consist of five main subsystems which include the transmitter, receiver, detector, data, and safety system. These subsystems were integrated and installed in a modified 8' x 20' x 8.5' shipping container to produce a mobile lidar laboratory. The table that holds the transmitter, receiver, and detector is shown in Figure 1 [21].

The transmitter, located on the bottom shelf, consists of a 1.5 joule Nd-YAG laser, with a primary wavelength of 1064 nm, manufactured by Continuum. This laser is Q-switched to provide high energy in short pulse lengths, approximately 7 ns, at a repetition frequency of 20 Hz. The primary wavelength is passed through frequency doubling and tripling crystals to produce the second and third harmonic wavelengths 532 nm and 355 nm. A small portion of the laser pulse energy, less than 0.5% in both 532 nm and 355 nm wavelengths, is lost from the beam by transmission and scattering at the first turning mirror. This lost transmitted beam energy is measured with a pulse by pulse energy monitor at the 355 nm and 532 nm wavelengths. The energy information is sent to the data collection unit and stored in the data file. The laser pulses are directed into a beam expander to reduce the divergence of the beam by 5X. After expansion the laser beam is directed by a micrometer driven steering mirror onto the horizontal axis of the lidar receiver. The beam is reflected by one other mirror and sent into the atmosphere.

The returning scattered laser light from the atmosphere is directed by a 24" optical flat mirror into a 16" classical Cassegrain telescope which is set up in the prone position.

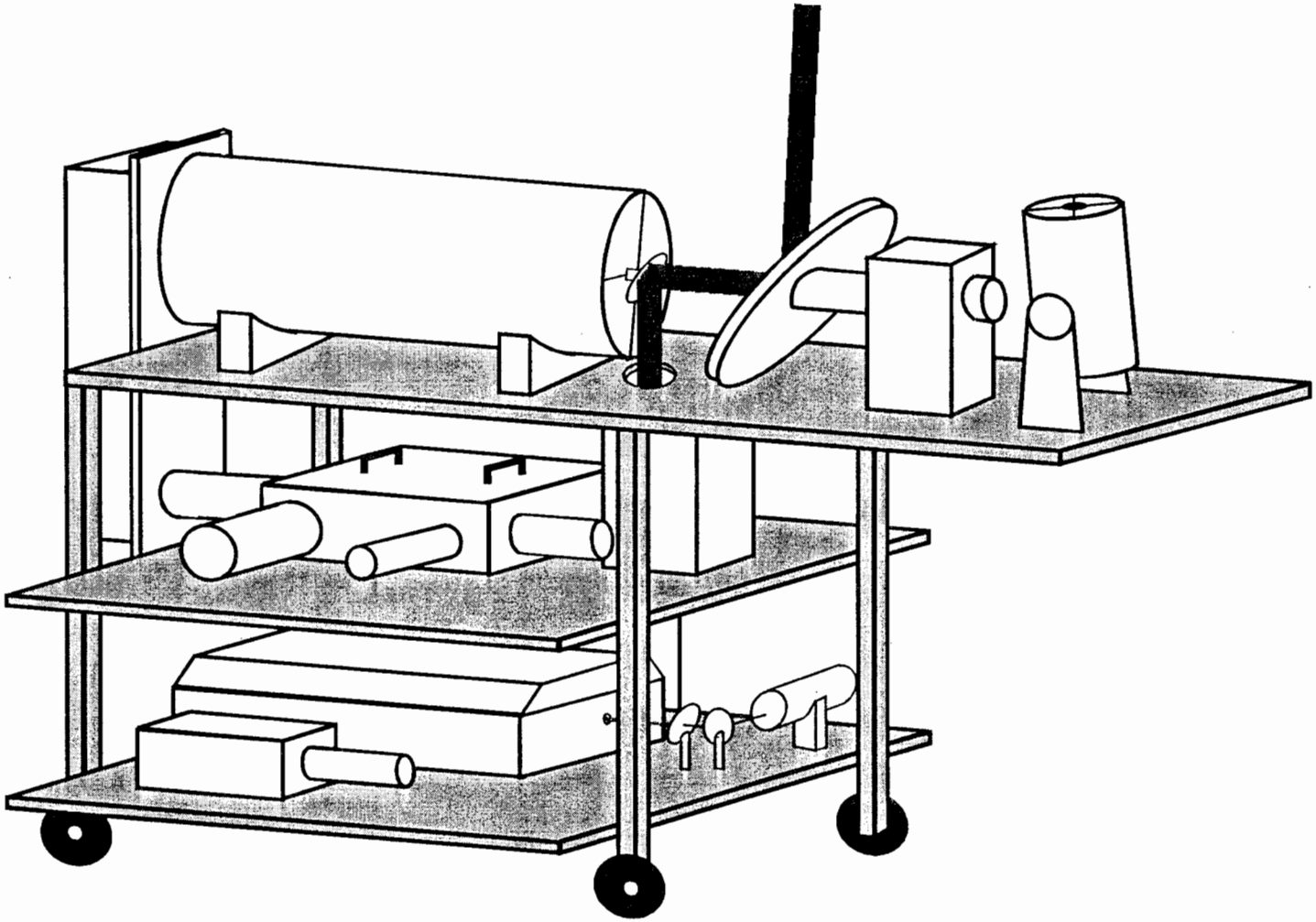

Figure 1. Drawing of the LAMP instrument and three of its five subsystems: transmitter, receiver and detector[21].

The telescope is set up in the horizontal position to minimize dust settling on the primary mirror, thus reducing cleaning and maintenance time. Before it enters the primary detector box, the light is focused and sent through a number of processing optics. The amount of background light incident on the potodetectors is reduced by placing a field stop at the prime focus to narrow the field of view of the telescope. Following the field stop, a Fabry lens, in combination with the negative secondary telescope mirror, forms a real image of the primary mirror. This produces a uniform distribution of all rays which strike the primary mirror within the field of view.

The light from the primary receiver is collimated and directed into the primary detector box where it first proceeds through a shutter wheel to pass all of the light from the ground to 85 km. The light is then split and filtered into four paths, one for each of the fundamental laser wavelengths, 355 nm and 532 nm, and one for each of the Raman scattered wavelengths, 607 nm and 660 nm. Approximately 1% of the fundamental wavelengths, 355 nm and 532 nm, is passed for the low altitude measurements, while the remainder of the signals are retained for the high altitude detection. The high altitude light is redirected back through a second slit in the shutter wheel to block out the high intensity light received from below 15 km. This prevents saturation of the high altitude photomultiplier tubes (PMT's). Light in the high altitude and Raman channels is photon counted, while light in the lower altitude channels is digitized.

A secondary receiver uses an 8" Schmidt cassegrain telescope to measure 532 nm light returns from the altitude range between 10 km and 50 km. Light from this receiver is focused into a 1 mm optical fiber and sent to a secondary detector box. This overlap

data provides a smooth transition between the high and low altitudes.

Data from the two detector boxes are sent to a CAMAC unit where it is averaged in one minute intervals (1200 laser shots) and stored on optical disks. Each of these channels is also averaged in thirty minute intervals and stored on the optical disks.

The timing of the lidar system comes from the shutter wheel which is run at a constant speed of 4800 rpm by a synchronous motor. The velocity of the shutter wheel controls the 20 Hz laser repetition rate. The shutter wheel rotates 16 times to complete a one shot sequence which includes 14 background samples, one laser shot, and one energy monitor sample. The 14 background samples are taken to average the noise in the signal-to-noise ratio.

Chapter 2

LIDAR EQUATION

The number of expected photons returning from a scattering volume depends on atmospheric conditions, scattering probability, and the various lidar subsystems. The lidar equation for Rayleigh and Raman scattering is,

$$N(R) = \frac{E_L}{hc/\lambda_L} * T(\lambda_L, R)\, T(\lambda_s, R) * \frac{\sigma(\lambda_L, \lambda_s)\, n(R)\, \Delta R}{4\pi} * \frac{\xi(R)\, A_o}{R^2} * \eta_{eff}(\lambda_s)$$

(1) (2) (3) (4) (5) (6)

where the terms of the equation are,

(1) number of scattered photons collected,

(2) number of laser photons transmitted,

(3) atmospheric transmission at the transmitted and received wavelengths,

(4) scattering probability in the integrated scattering volume,

(5) probability of reception from the scattering volume,

(6) optical efficiencies of the lidar detector and data system,

and the parameters of the equation are,

N(R)	=	number of photons returning from altitude z,
E_L	=	laser pulse energy,
h	=	Planck's constant,
c	=	speed of light,

λ_L	=	emitted laser wavelength,
λ_S	=	scattered wavelength,
$T(\lambda_L, R)$	=	atmospheric transmission for λ_L at altitude R,
$T(\lambda_S, R)$	=	atmospheric transmission for λ_S at altitude R,
$\sigma(\lambda_L, \lambda_S) / 4\pi$	=	backscattering cross section for incident wavelength λ_L and emitted wavelength λ_S,
$n(R)$	=	atmospheric number density at altitude R,
ΔR	=	integration range,
$\xi(R)$	=	probability that light scattered from range R will reach the detector, based on geometric considerations,
A_O / R^2	=	acceptance solid angle of the receiver optics (A_O = area of objective mirror),
$\eta_{eff}(\lambda_L)$	=	optical efficiency of the lidar instrument and geometric efficiencies of the detector system.

The general properties of scattering and atmospheric transmission will be addressed in this chapter. The other factors in the lidar equation will be addressed in subsequent chapters, since they relate to specific aspects of the LAMP lidar system.

2.1 Scattering

The three types of scattering important to the LAMP lidar are elastic molecular, particle, and Raman. Each of these types are visually depicted in Figure 2. An important term in the lidar equation is the backscatter cross section, which signifies the probability per steradian that a molecule will scatter light back in the receiver direction. The value of the cross section has been well documented for various molecules; little error will be

Elastic molecular scattering (Rayleigh)

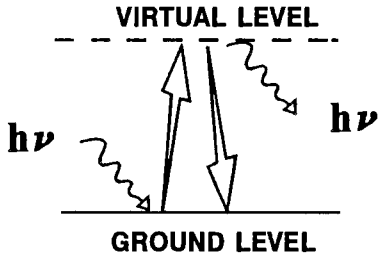

Particle scattering (Mie)

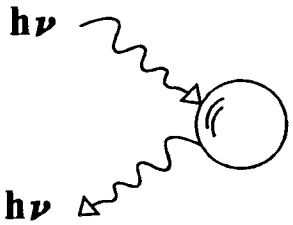

Inelastic molecular scattering (Raman)

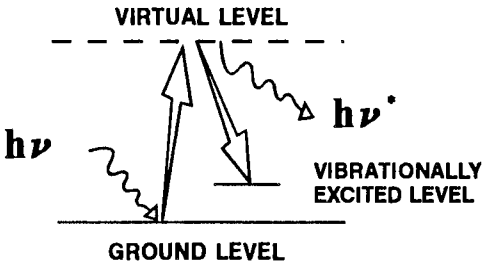

Figure 2. Scattering techniques experienced in the LAMP lidar.

introduced into the computed return as a result of this parameter. The relative intensities of the backscatter cross section for the various types of scattering are shown in Figure 3 [10]. The differences in intensities determine the types of measurements that can be performed. Table 1 lists the cross sections for Rayleigh and Raman scattering for several atmospheric constituents [10].

Table 1. Backscatter cross sections for Raman and Rayleigh scattering for various atmospheric constituents.

Molecule	Backscatter Cross Section (10^{-31} cm^2 / sr)			
	Rayleigh Scattering		Raman Scattering	
	355 nm	532 nm	From 355 nm	From 532 nm
Air	31400	6225.9	---	---
N_2	31310	6208	22.8	5.64
H_2O	---	---	63.42	12.57
O_2	26340	5222	37.4	7.416

A. Rayleigh Scattering. Rayleigh scattering consists of both elastic scattering on the Cabannes line, which occurs when the scattering molecules are much smaller than the wavelength exciting it, and Raman scattering associated with the rotational states, Stokes and anti-Stokes, on either side of the Cabannes line [27]. The elastic part of Rayleigh scattering, which is of prime concern for the LAMP lidar, occurs when a photon raises a molecule to a virtual energy state and the molecule reradiates a photon at the same frequency. The spectral line reradiated by a large number of molecules is

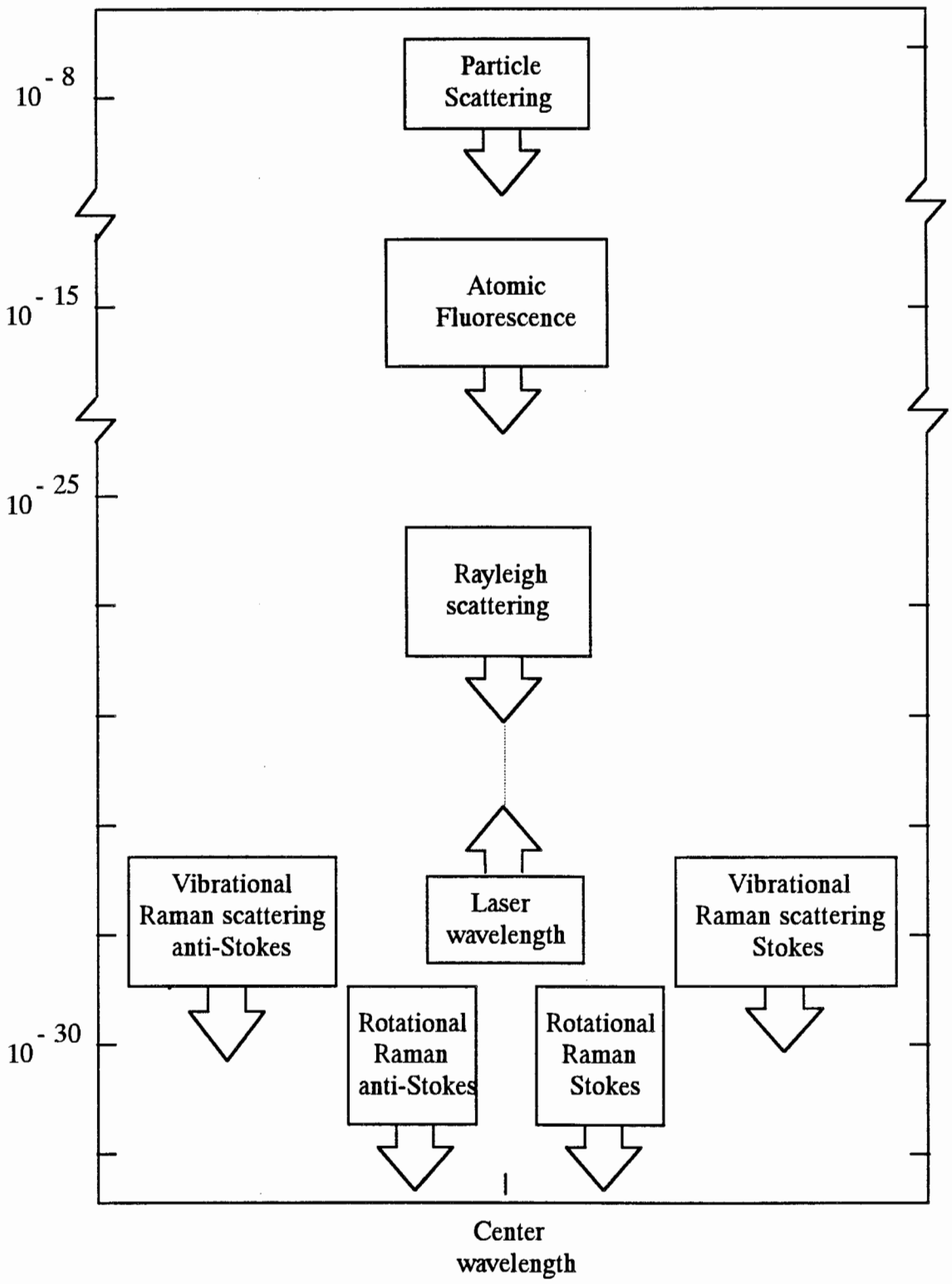

Figure 3. Backscatter cross sections for several scattering techniques [10].

broadened to the Doppler width corresponding to their thermal motion. The backscatter cross section for elastic Rayleigh scattering is,

$$\sigma_{\pi}{}^{R} = \frac{\pi^2 (n^2 - 1)^2}{N^2 \lambda^4}, \tag{2}$$

where,

n = index of refraction,

N = number density of scatters,

λ = scattering wavelength.

It is important to note that the backscatter coefficient depends on λ^{-4}. Thus, 355 nm light is 5 times more susceptible to molecular scattering than 532 nm light. This allows a scattered 355 nm photon to be detected at higher altitudes than a 532 nm photon. Rayleigh scattering is the technique used for density and temperature measurements at high altitudes where no significant dust or aerosol scattering exists [16].

B. Aerosol Scattering. Aerosol scattering occurs when the irradiated particle is of a similar or greater size than the wavelength of the incident photon. This is an elastic scattering process, so the spectrum of the scatted light is similar to that of the transmitted laser pulse. Since the thermal velocity of such a particle is small, there is little Doppler effect on the frequency of the scattered light. Figure 3 shows that aerosol scattering is 18 orders of magnitude greater than molecular scattering, and 21 orders of magnitude greater than Raman scattering. Thus, in the presence of aerosol scattering, the intensity of the returning light can be high enough to render any direct molecular

measurements useless [10]. However, if several different wavelengths are being transmitted, the returning intensities can be used to characterize the particle and molecular scattering contributions, as shown in Figure 4a [22]. The dashed line signifies the modeled molecular profiles which overlap the measured profiles obtained from the 355 nm and 532 nm lidar channels. Aerosol scattering dominates the measured signal which deviates substantially from the molecular profile in the lower atmosphere. Figure 4b shows the ratio of 532 nm backscatter intensity to 355 nm backscatter intensity. It is relatively constant at two different values through the stratosphere, indicating that two particle size distributions exists. The equation for the backscattering coefficient of aerosol scattering is very complex because atmospheric particle scatterers vary in composition, index of refraction, size, and shape [10]. Mie scattering theory can be applied to describe the scattering process. (See Derjimenem, van der Hulst, and Borhen for discussion of the Mie theory as applied to aerosols.) In general it is difficult to separate the scattering factors associated with size distribution, concentration, and particle shape.

C. Raman Scattering. Raman scattering is an inelastic molecular scattering process, where a photon excites a molecule to a virtual level, and the molecule reradiates a photon at a different frequency from the original frequency. This emitted photon has a frequency unique to the scattering molecule. The shift can either fall on the Stokes, lower energy, or anti-Stokes, higher energy, side of the initial photon frequency. Raman shifting can be either rotational or vibrational in origin. Vibrational shifting results in a shift in the order of 10's to 100's of nanometers from the central wavelength, while

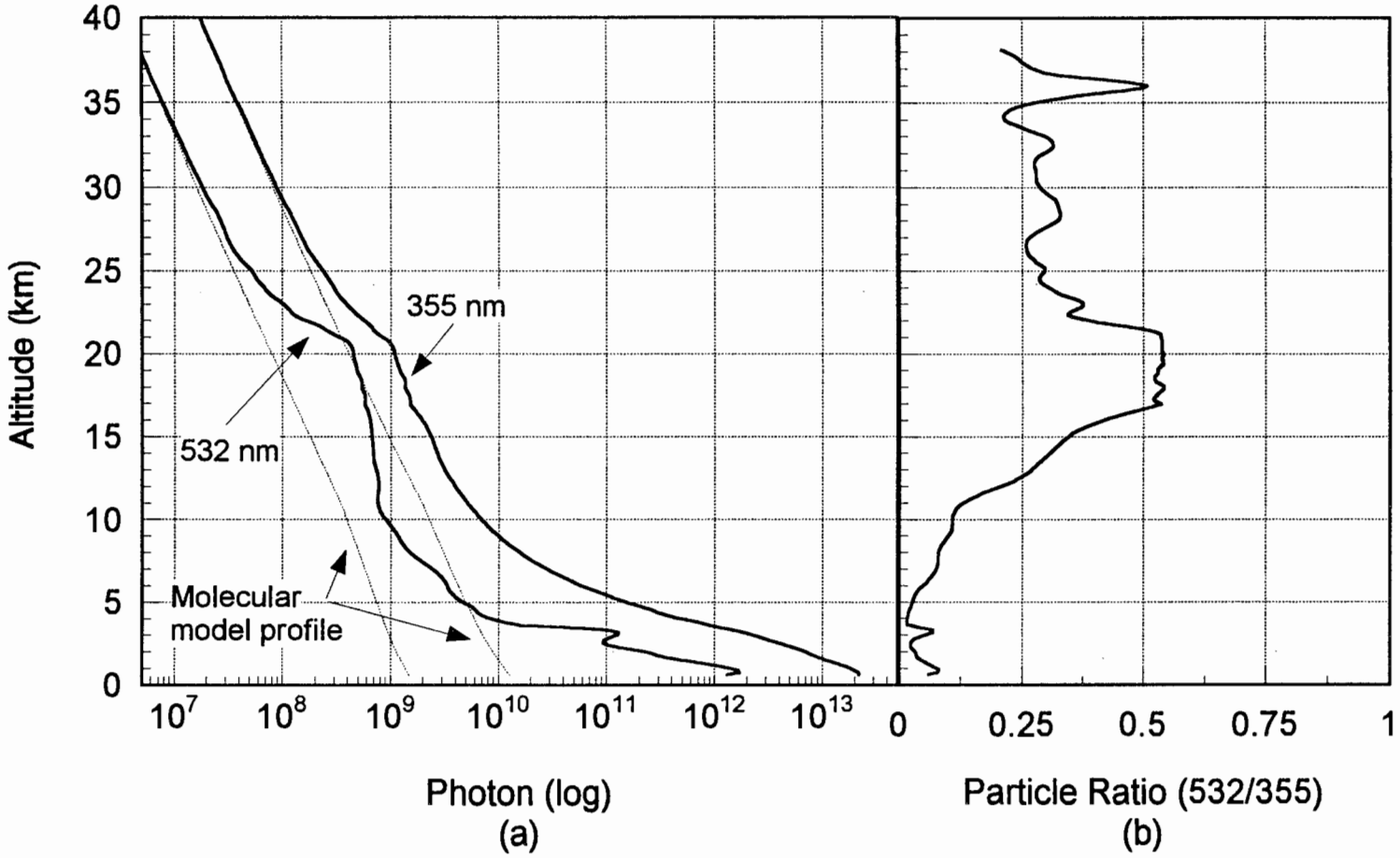

Figure 4 Two color lidar return with calculated particle size distribution. Part (a) shows stratospheric and tropospheric relative density profiles with high backscatter intensities measured by the 355 nm and 532 nm LAMP data channels. Part (b) shows particle size distribution found by taking the ratio of the 532 nm profile to the 355 nm profile. Measurements taken aboard the RV Polarstern on 22 November, 1991 [22].

rotational shifting can result in shifts of 1's to 10's of nanometers and depends on the temperature of the molecule. Figure 5 shows vibrational and rotational shifting pertinent to the LAMP lidar. The intensities of the vibrational lines are typically three orders of magnitude lower than that of the central frequency, and the magnitudes of the rotational states are typically two orders of magnitude lower than the central "Q" branch. Thus, measurements of the vibrational shifted wavelengths require long integration times. The advantage of Raman scattering over Rayleigh scattering is that it is specific to the molecule, and is not overpowered by the aerosol scattering of the lower atmosphere, assuming that the filters can reject the fundamental laser frequencies. Temperatures can be calculated directly from the relative density profiles, in a like manner to the high altitude Rayleigh scattering. However, the Raman signal is subject to extinction from aerosols which can present a problem in the presence of clouds. An example of this extinction is shown in Figure 6 for a nitrogen channel data set of the LAMP system. The signal deviates from the straight molecular profile at 8.5 km, where cloud backscatter is shown in the 532 nm data file. Correction for this extinction allows for direct measurements of density, and thereby temperature.

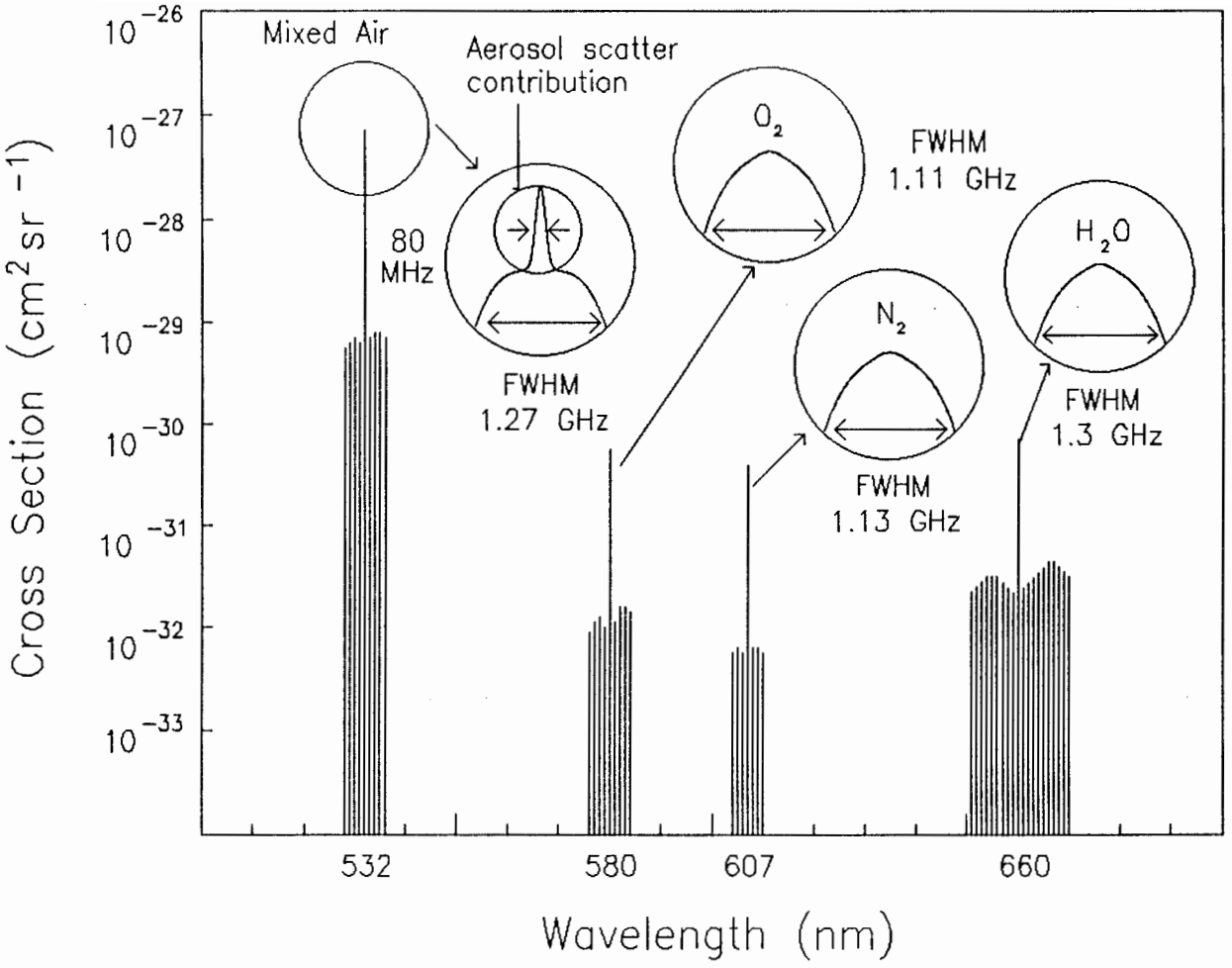

Figure 5. Raman shifts from the 532 nm primary wavelength used in the LAMP lidar.

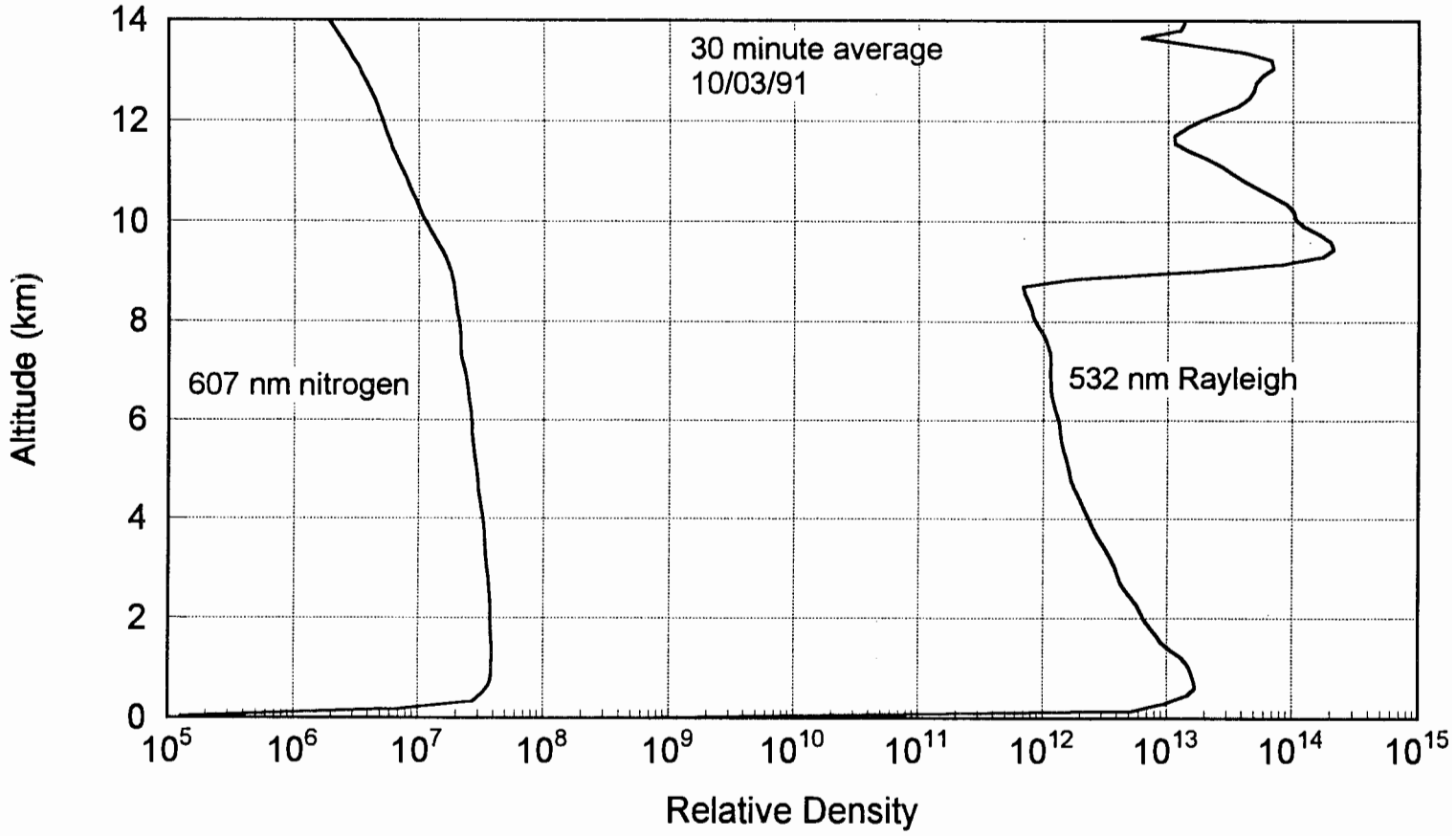

Figure 6 Extinction in the Raman shifted nitrogen channel caused by high intensity praticle layers as seen in the 532 nm backscatter profile

2.2 Atmospheric Transmission

The atmospheric transmission is the most unstable variable in the lidar equation. The characteristic decrease in transmission from low altitudes to high altitudes can be explained by molecular scattering, and by aerosol scattering due to meteorological conditions, pollution, and volcanic eruptions. As a result of the chemical composition of the atmosphere, certain wavelengths of light are subject only to scattering processes, while at other wavelengths there will be significant absorption. Figure 7 shows a plot of the atmospheric transmission of the Earth over a spectral range corresponding to the peak in solar radiation [25]. In each of the absorption bands the primary chemical absorber is listed.

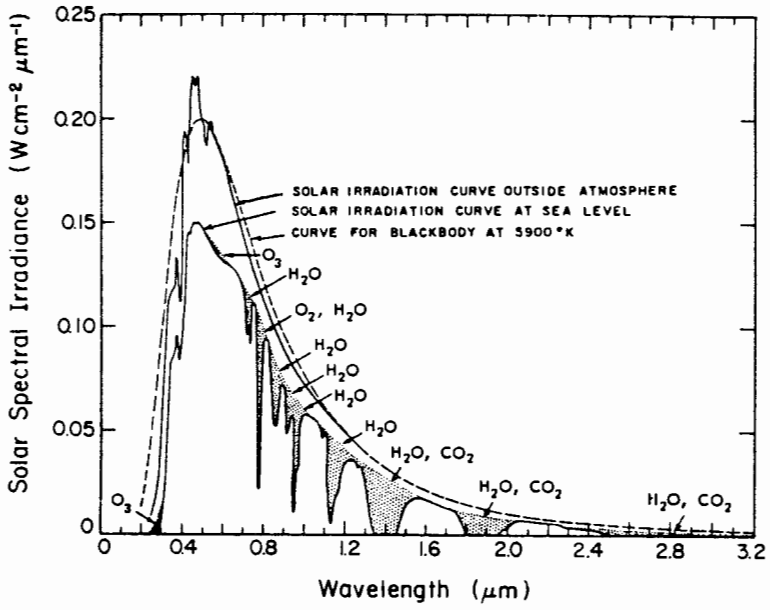

Figure 7. Atmospheric spectral transmission for the Earth from direct sunlight [25].

If the concentration of a molecular species associated with an absorption band is altered, an attenuation or amplification of the originally calculated return intensity will occur. Thus, if one were to operate a UV lidar in a region where significant ozone depletions occur, one would expect to obtain a higher return from a given altitude.

Water vapor concentration in the atmosphere causes most of the variability in meteorological conditions. If there is only a light haze in the atmosphere, only a small portion of the transmitted and scattered light from a lidar system will be attenuated. Heavy cloud cover, on the other hand, can eliminate any transmitted or returned signal from altitudes above the scattering cloud layer. A plot of such high attenuation from cloud cover is shown in Figure 8 for the 532 nm high and low altitude data channels. Immediately following the large scattering layer, the low altitude signal drops off to background level. The cloud has scattered and absorbed all of the laser light so that the normal return from the high altitude regions cannot be observed. In this example the data profile was cut off at a signal statistical error of 10%, so the high altitude channel only received data to 16.5 km. With a clear sky the LAMP system can record returns from altitudes up to 80 km.

Most pollution resides in the lower atmosphere from the ground to approximately 2 km (boundary layer). The number and size of aerosols in this layer are sufficiently large enough that aerosol scattering dominates at the transmitted wavelength. The boundary layer usually causes two effects in the expected photon return, low altitude signal enhancement from aerosol backscattering, and reduction of the laser beam intensity at high altitudes. Large enhancements from aerosol backscattering can saturate the signal

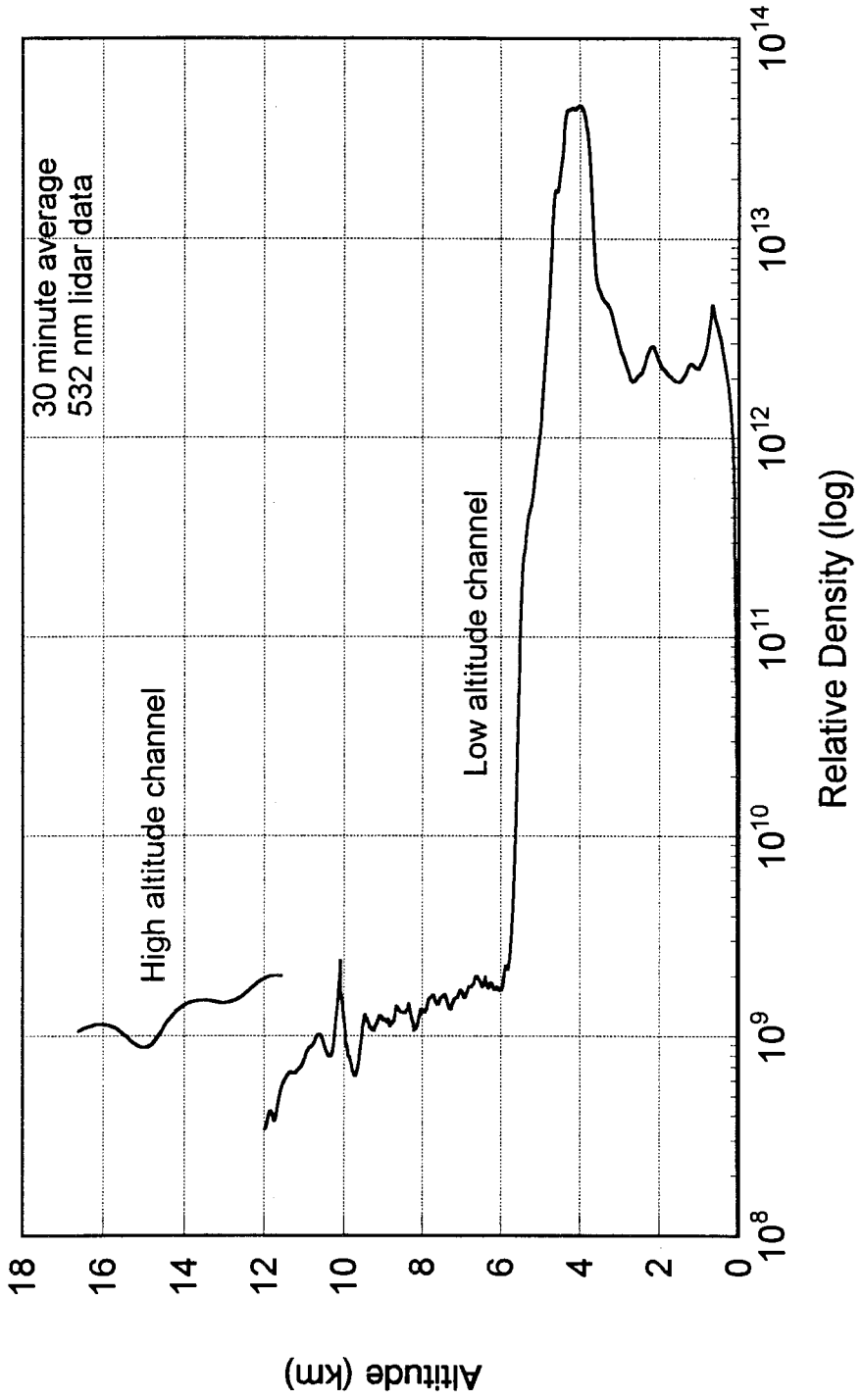

Figure 8 High level extinction from heavy cloud coverage on the 532 nm high altitude data channel. Data was taken aboard the RV Polarstern on November 15, 1991.

and possibly damage PMT's. Extinction of the transmitted beam by aerosols will lower the signal from higher altitudes.

The upper stratosphere also contains a significant amount of aerosols. They are mainly H_2SO_4 created from the SO_2 flux of the volcanic eruptions. These eruptions send tons of ash into the stratosphere and cover the globe in a matter of months. In 1982 El Chichon sent ash to heights of 38 km. The ash settled out within a few months and the remaining aerosols had decreased to a low level when the larger eruption of Mt. Pinatubo occurred in July 1991. The Pinatubo eruption sent the most ash recorded in this century into the atmosphere. Its ash circled the globe in about three weeks [23] and most of it settled out within two months. The aerosols are expected to remain at significant levels for the next five to ten years. Figure 9 shows a sample of data from the LADIMAS campaign of the stratospheric aerosol layer at 5° S latitude on 29 November, 1991. This plot shows a signal enhancement of 18 times the modeled molecular profile, indicating large extinction values of the transmitted and received signals from higher altitudes.

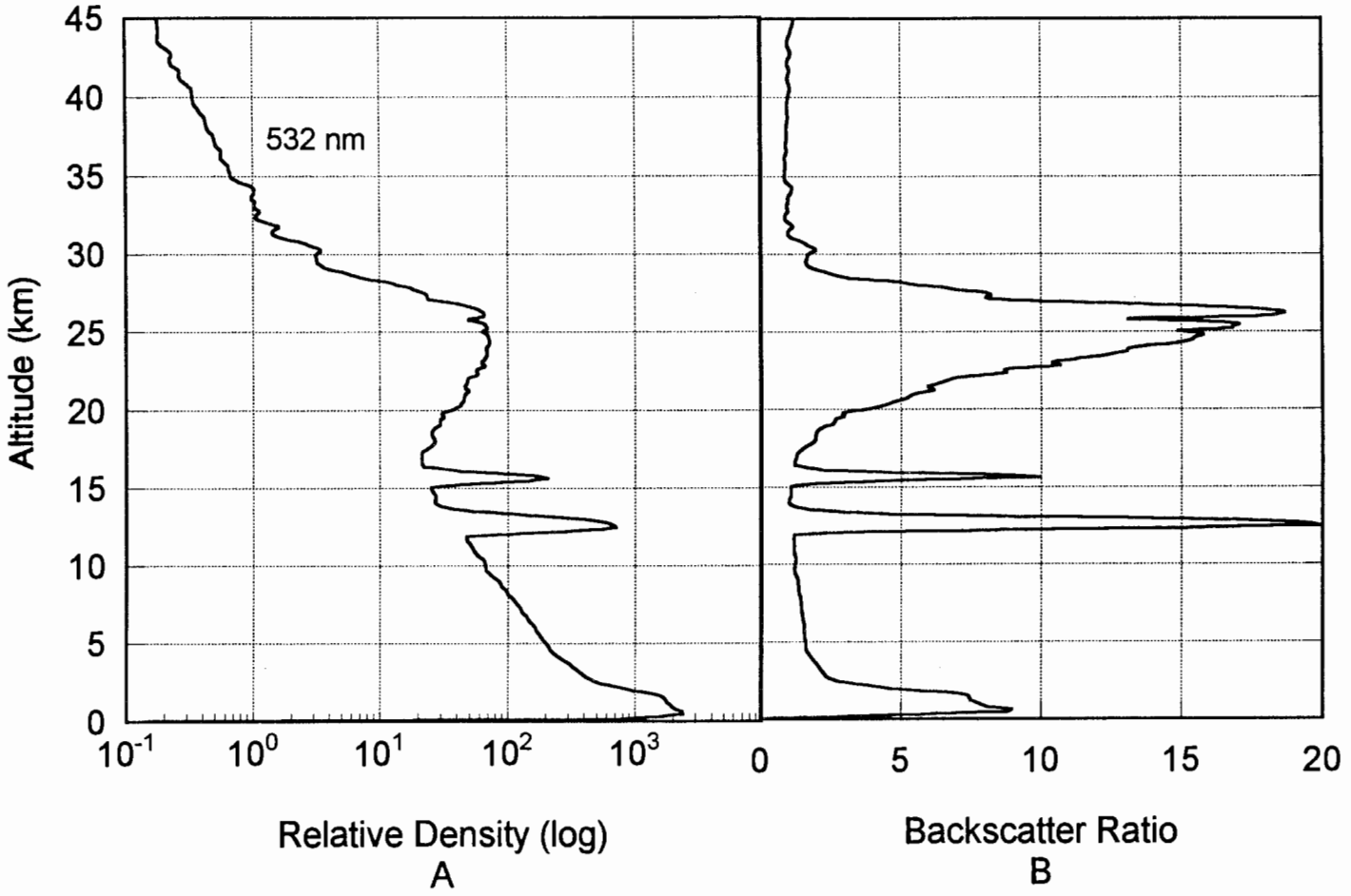

Figure 9. Stratospheric aerosol layer measured by the LAMP lidar while aboard the RV Polarstern on 29 November, 1991, at 5 degrees south latitude. The backscatter ratio was calculated by taking the ratio of the molecular scattering to the aerosol scattering.

Chapter 3

RECEIVER PROBABILITY

From the lidar equation, the receiver probability was defined as $(\xi(R) \cdot A_O) / R^2$, where $\xi(R)$ is the probability that light scattered at altitude R will reach the receiver, based on geometric considerations, and A_O / R^2 is the receiver acceptance solid angle. This chapter will discuss the effects of geometry on the receiver probability and the modeling of LAMP lidar performance using various telescope fields of view.

The receiver system for the LAMP lidar is shown in Figure 10 [21]. The scattered light returning from the atmosphere is directed by a 24" flat mirror into a 16" classical Cassegrain telescope. The telescope collects the light and directs it through beam-steering and processing optics. A field stop in the focal plane of the telescope narrows the field of view and reduces background noise. The light passes through a Fabry lens which images the primary mirror. Using the Fabry lens has the advantage of spreading the intensity of the incoming beam over the entire image and not just concentrating it at the center, as in the case of the infinity image focus. This light intensity provides for uniform distribution of the signal over the active face of the PMT photocathode. Once past the Fabry lens the beam is collimated and sent to the detector system.

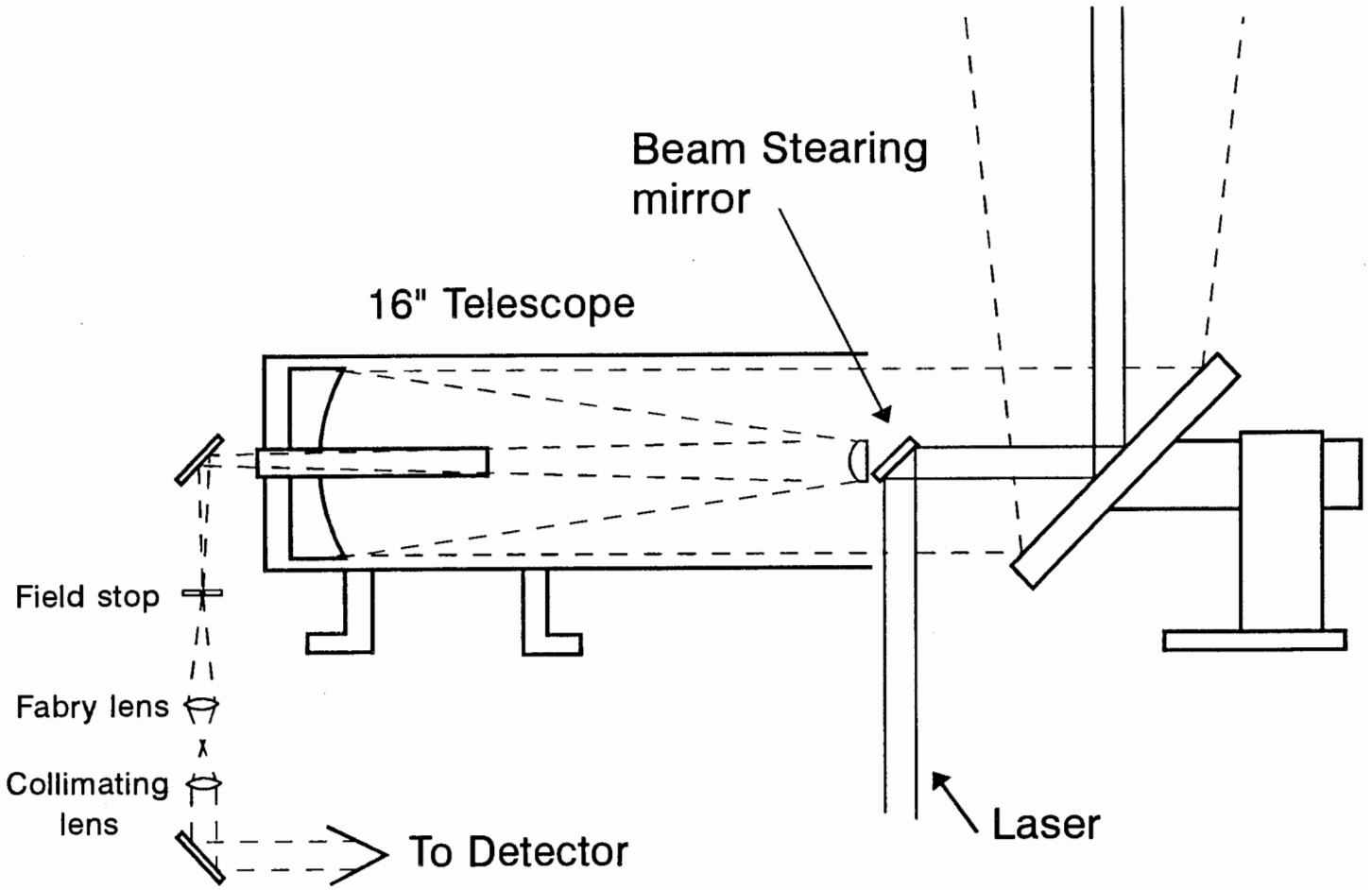

Figure 10. Drawing of the optical ray path through the receiver system. The position of the field stop and following two beam forming lenses is shown with respect to the 16" Cassegrain telescope and 24" collecting flat [21].

3.1 Geometric Considerations

If all optical obstructions and geometric considerations were neglected, the receiver probability would be based solely on the acceptance solid angle of the objective mirror of the Cassegrain telescope. This is shown in Figure 11.

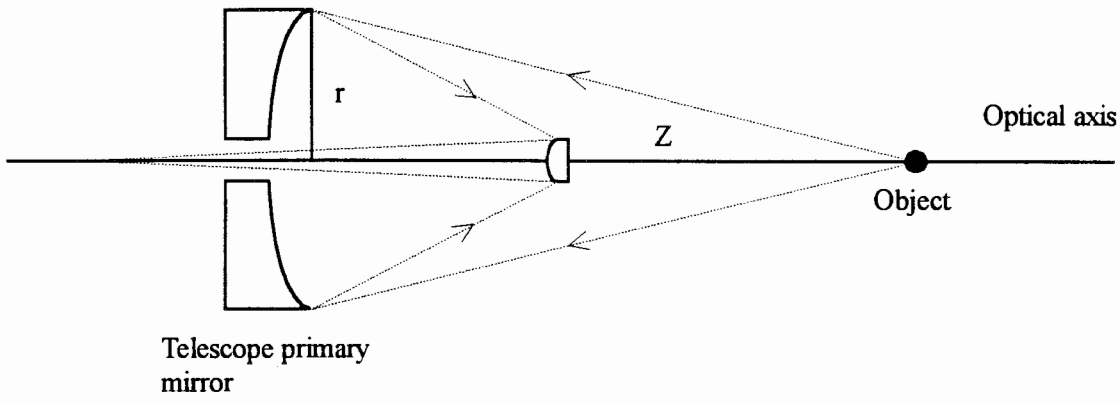

Figure 11. Acceptance solid angle for the receiver of a lidar system

In actual lidar systems the three main factors which can reduce the effective acceptance solid angle are centering of the laser beam in the field of view of the telescope, shifting telescope alignment, and shifting of the near-field image plane.

A. Field of View. The transmitted laser beam must be coaxial with the field of view of the telescope. The alignment must be checked at the beginning of each measurement session, since there is a tendency for small vibrations or thermal effects to

alter the alignment. Alignment is performed with a mechanical beam steering unit, on the secondary mirror mount of the telescope, controlled by motor micrometers. Alignment is possible through adjustments of the micrometers, of the order of a few microns, on the two axes of rotation. Although the LAMP lidar did not have an automatic alignment control system on the LADIMAS campaign, it will be fitted for one in the near future.

B. Telescope Alignment. Vibrations may cause the receiving telescope to lose its alignment. The location of the optical axis in the focal plane will be shifted from its original location as seen in Figure 12. The telescope has been represented as a single lens for simplicity. The angle of misalignment has been exaggerated for clarity.

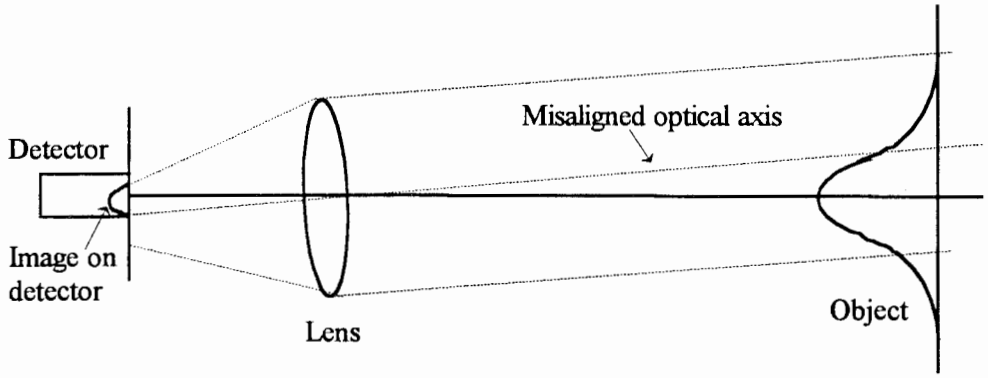

Figure 12. Attenuation effects on the signal due to telescope misalignment.

Misalignment may result in a truncated image if the field of view of the telescope is not large enough to capture the entire object. An automated field of view control system may try to compensate for this misalignment, but there will still be loss due to obstructions in the telescope, such as the housing, secondary mirror, and baffles. Even if the field of view is large enough, the detector aperture may not be large enough to receive the displaced image. For an instrument which is constantly being transported, stiff telescope mounting structures are recommended.

C. Near-Field Image Plane. As measurements are taken closer into the near field, the focal plane of the telescope begins to shift so that the image distance becomes longer, as shown in Figure 13.

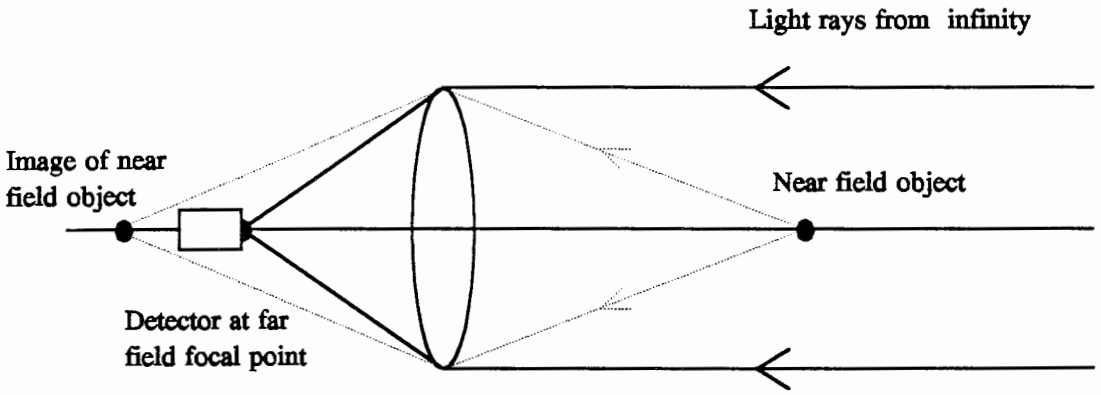

Figure 13. Image point of a near field object by a telescope focused at infinity.

As the focal distance increases, the field stop begins to act as an aperture stop, cutting down the amount of light the detector receives. Light rays from the outer part of the primary mirror fall on the far field focal plane, beyond the field stop. Part of the near field signal becomes blocked from passing through the detector system. Figure 14 shows the image size (dashed lines) for various altitudes superimposed on the field stop opening (solid line).

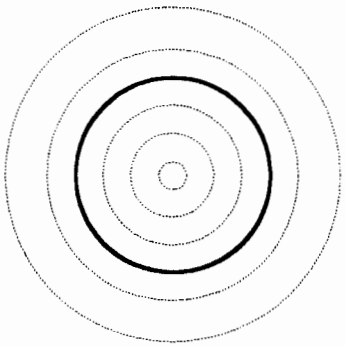

Figure 14. Near field image size of an object (dashed lines) superimposed on the field stop opening (solid line).

With perfect alignment of the laser beam and the telescope, this near-field phenomenon could be corrected by geometric calculations. However, if there is a drift in the field of view, the image circles will be skewed relative to the field stop, causing nonlinear signal attenuation.

3.2 Telescope Modeling

Telescope vignetting, caused by near field imaging, has been modeled. The compounded effects of the field of view of the telescope, laser beam divergence, assumed Gaussian cross section of the laser beam, telescope obstructions caused by the secondary mirror, and aperture size must all be accounted for in the calculation. These calculations were performed by a program, written by Dan Lysak, to help model an expected return given the efficiencies of the receiver system. The specifications of the LAMP classical Cassegrain telescope are listed in Table 2. The principle of the program is to ray trace 1000 segments of the Gaussian laser beam from the scattering target to weighted areas on the telescope primary mirror, and count how many rays arrive inside the field stop. The altitude resolution for the calculations was set at 15 meters for the low altitude Rayleigh channels and 75 meters for the high altitude Rayleigh and low altitude Raman channels, simulating the range resolution of the LAMP lidar. The results of the model are shown graphically in Figure 15. An interesting point to note is that for a 1/4" aperture stop, the telescope begins to open at 90 meters and does not fully open until 500 meters. Thus if it is too difficult to account for misalignment effects, accurate data can not be collected below 500 meters.

Table 2. Classical Cassegrain telescope specifications of the LAMP lidar.

Classical Cassegrain Telescope of the LAMP Lidar	
Overall telescope specifications	
Focal length	240"
Back focal length	15.25"
Overall length	58"
Diameter	20"
Weight	115 lbs
Primary to secondary distance	44.38"
Primary mirror	
Focal length	60"
Diameter	16"
Secondary mirror	
Diameter	5"
Mirror obstruction	5.2"
Baffling	
Length	21"
Diameter	3"

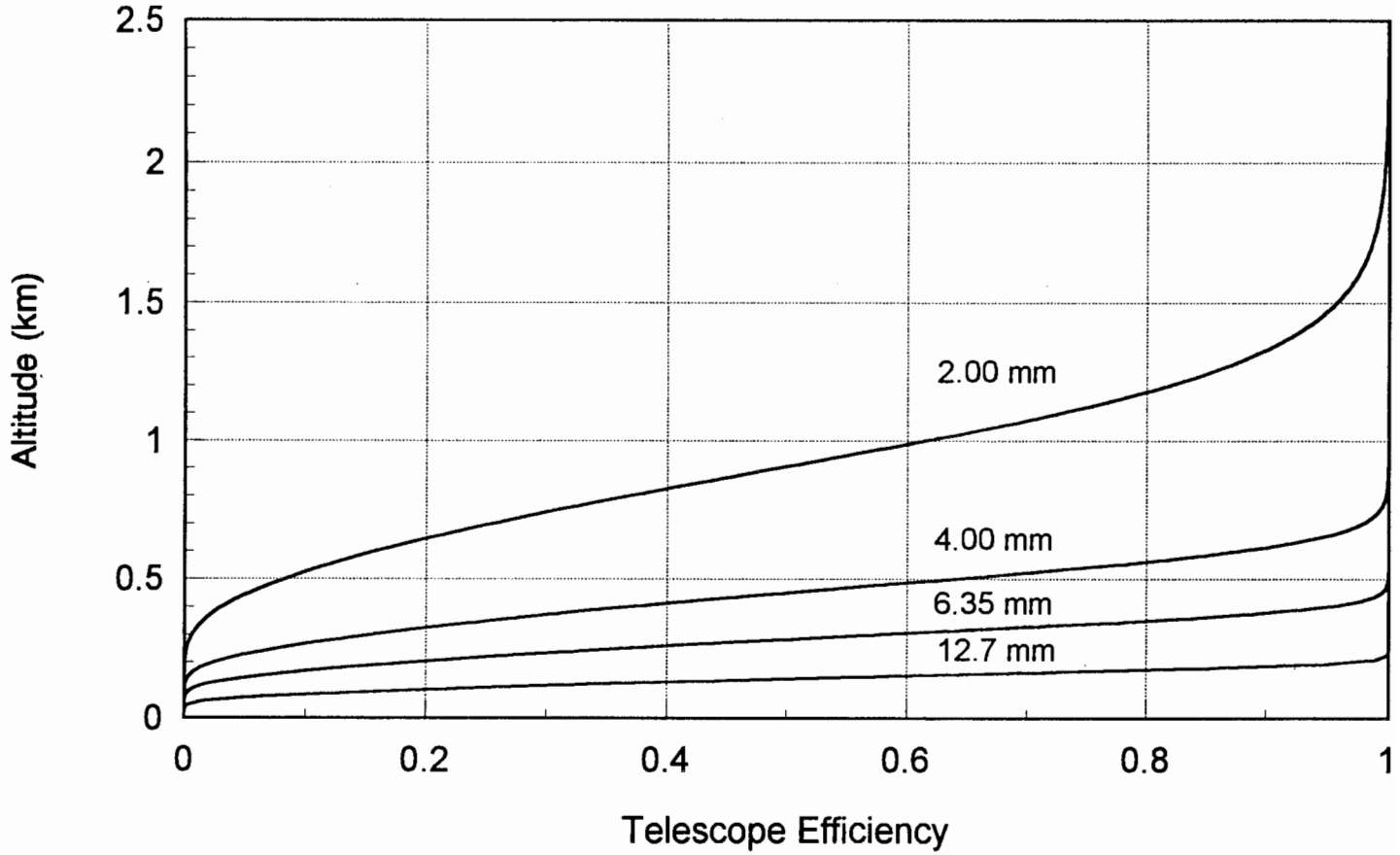

Figure 15. Near field telescope efficiencies for the classical Cassegrain telescope used in the LAMP lidar for various field stop sizes.

Chapter 4

OPTICAL PROPERTIES

Within any lidar system, there are many optical properties and materials that can contribute to the loss of returning photons. These effects become increasingly significant as the number of optical components in a system increases. The LAMP system, for example, has a total of 25 optical components in the 532 nm high altitude channel. Special care is needed to maximize the transmission through lenses and reflection by the mirrors for each of the detected wavelengths. A number of these optical properties will be reviewed to explain some of the limitations of the LAMP lidar. Reference has been made to the Optics Guide 4 catalog published by Melles Griot [14].

4.1 Reflection and Transmission Fundamentals

The most important properties for lenses and mirrors in a Raleigh/Raman lidar system are internal and external reflectance and transmittance, polarization by a surface, refractive index, and optical coatings. Except for the refractive index, an inherent property of a material, all of the above processes can be calculated with Fresnel equations. These equations explain the propagation of light at the boundary of a dielectric media, as seen in Figure 16.

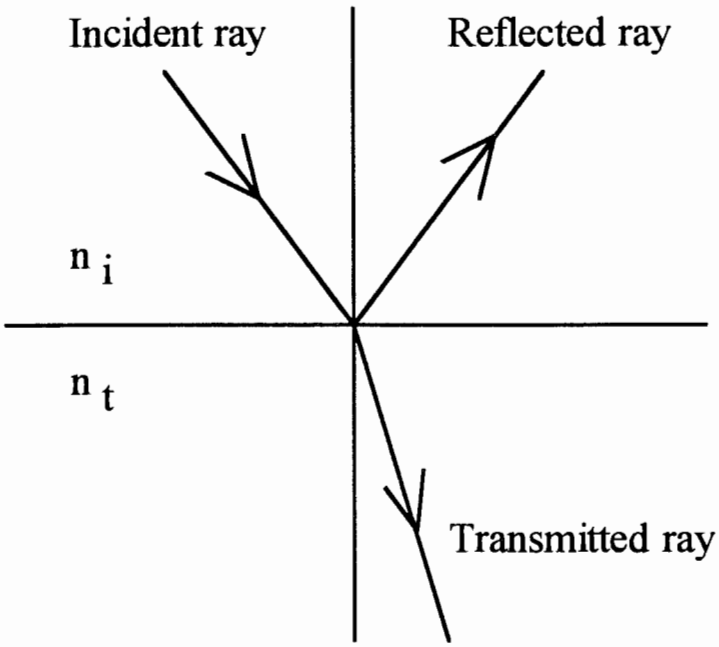

Figure 16. Light propagation at a dielectric interface..

Both amplitude and phase can be determined for the incident, reflected , and transmitted rays. Without going into the derivation, the Fresnel equations for parallel (subscript p) and perpendicular (subscript s) polarizations, relative to the plane of incidence, are,

$$r_s = \frac{n_i \cos\theta_i - n_t \cos\theta_t}{n_i \cos\theta_i + n_t \cos\theta_t}, \quad (3)$$

$$r_p = \frac{n_t \cos\theta_i - n_i \cos\theta_t}{n_i \cos\theta_t + n_t \cos\theta_i}, \quad (4)$$

$$t_s = \frac{2 n_i \cos\theta_i}{n_i \cos\theta_i + n_t \cos\theta_t}, \quad (5)$$

$$t_p = \frac{2 n_i \cos\theta_i}{n_i \cos\theta_t + n_t \cos\theta_i}, \quad (6)$$

where the parameters of the equations are,

r_s = amplitude reflection coefficient for perpendicularly polarized light,
r_p = amplitude reflection coefficient for parallel polarized light,
t_s = amplitude transmission coefficient for perpendicularly polarized light,
t_p = amplitude transmission coefficient for parallel polarized light,
n_i = incident medium index of refraction,
n_t = transmitting medium index of refraction,
θ_i = incident angle relative to normal,
θ_t = transmitting angle relative to normal.

A. Reflectance. Fresnel's equations show that the reflectance of a surface is dependent on the index of refraction of the two media, the angle of incidence of light striking the surface, and the polarization of the light. External reflection occurs on transition from a low index to a high index of refraction ($n_t/n_i > 1$). Internal reflection involves transition from a high index to a low index of refraction ($n_t/n_i < 1$). When a

light wave undergoes external reflection there is a 180° phase shift in the propagating wave. Internal reflection does not show any phase change except in the case of total internal reflection. Figures 17 and 18 show the reflectance of the p and s polarizations for both internal and external reflection from an air-glass interface, respectively. For both internal and external reflection, the reflectance for the two states of polarization are equal at low and high angles of incidence. Between these extremes of angles, the reflectance from the different states of polarization are noticeably different. These effects must be considered when designing an optical system. Two angles of interest on the reflectance curves are Brewster's angle and the critical angle.

Brewster's angle is the angle at which parallel polarized light is totally transmitted through the interface while leaving the reflected light perpendicularly polarized. This angle occurs at 56.3° for a air-glass interface with glass having an index of refraction equal to 1.5. Brewster's angle is given by Equation 7 and shown in Figure 19,

$$\theta = \arctan\frac{n_t}{n_i}, \tag{7}$$

θ = Brewster's angle of incidence,
n_t = transmitting medium index of refraction,
n_i = incident medium index of refraction,

If polarized light must pass through a window, Brewster's angle can be used to reduce reflections instead of using an anti-reflective coating.

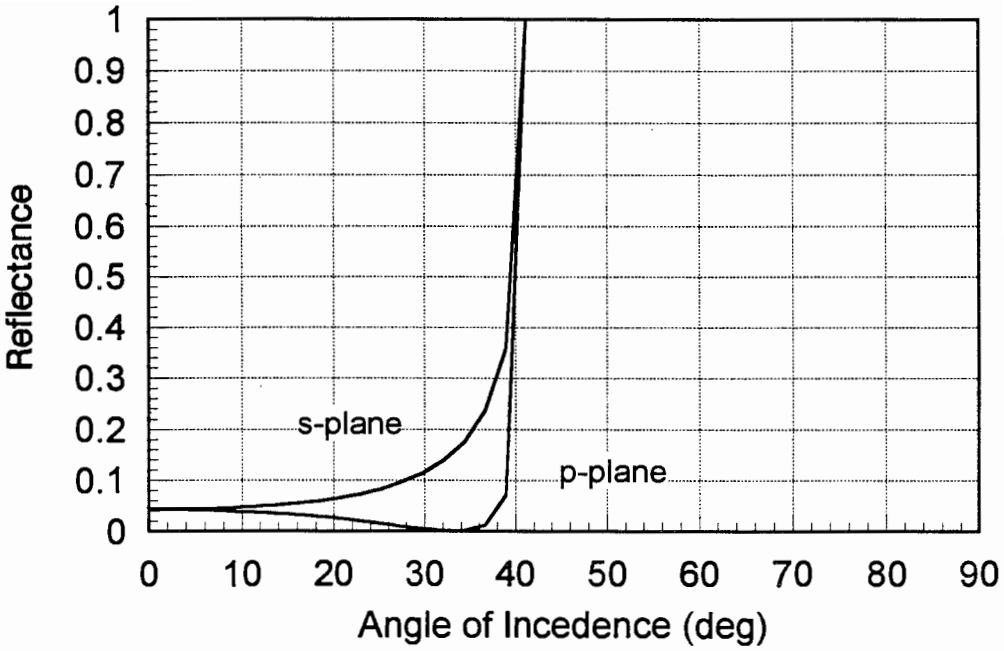

Figure 17. Internal reflectance for p and s polarization at varying incident angles.

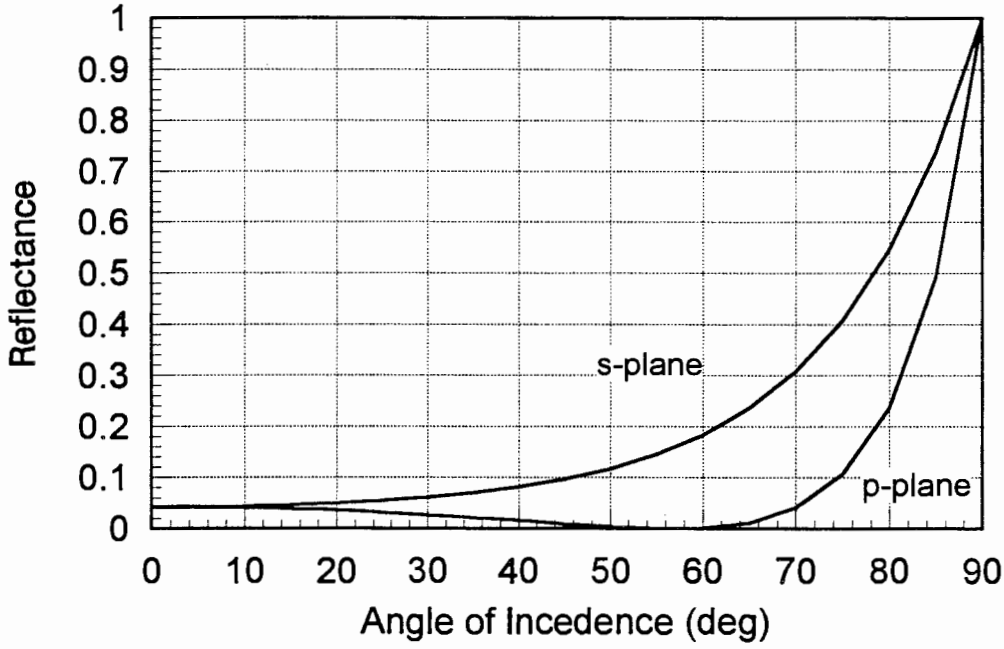

Figure 18. External reflectance for p and s polarization at varying incident angles.

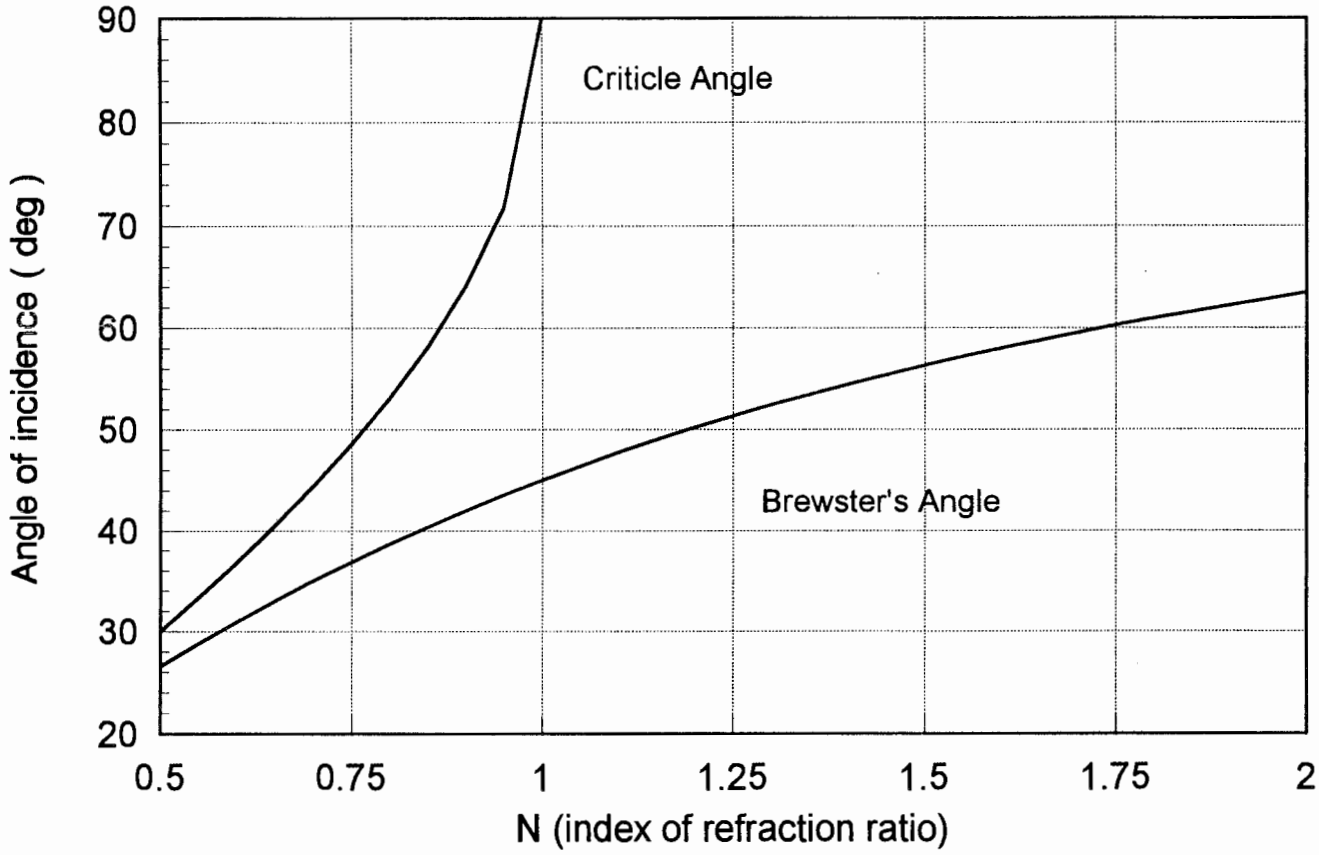

Figure 19. Brewster's and the critical angle as a function of the ratio of index of refraction of two materials.

The critical angle only occurs for internal reflection. It is the incident angle which results in total reflection, and is given by Equation 8, and plotted in Figure 19,

$$\theta = \text{arc sin}\frac{n_t}{n_i}, \tag{8}$$

θ = critical angle of incidence,
n_t = transmitting medium index of refraction,
n_i = incident medium index of refraction.

B. Transmittance. Internal transmittance (T_i) is the fraction of light that can pass through a given amount of material, not including boundary losses. External transmittance (T_e) is the amount of light that passes through an optical element. Internal transmittance is a function of the absorption properties of the material,

$$T_i = e^{-\mu t_c}, \tag{9}$$

where μ is the absorption coefficient of the material, and t_c is the lens center thickness. External transmittance includes the effect of the two boundary interfaces,

$$T_e = t_1 t_2 T_i, \tag{10}$$

where t_1 and t_2 are the Fresnel transmission coefficients for the first and second interfaces. External transmittance is critical for image forming optics. Without anti-reflective

coatings, sharp interface angles must be avoided to preserve part of the signal. The incidence angle becomes critical in polarization measurements, since the reflectance is highly dependent on incident angle.

4.2 Anti-reflective Coatings

Anti-reflective coating techniques are based on the principles of reflectance and transmittance, section 4.1, and on the principle of interference. Anti-reflective coatings are used to reduce reflections off of an interface, thus increase transmission. This is possible because the principle of the conservation of energy states that the incident light must equal the transmitted light plus the reflected light, assuming no absorption by the material. Thus, if the interface reflections are canceled, all of the light will be transmitted through the material. Figure 20 shows the interfaces of a thin film overlaid on a substrate material.

Assume that the intensity for external reflectance is equal from all surfaces, and that $n_{air} < n_{ar} < n_{mat}$, where n_{air} is the index of refraction for air (= 1), n_{ar} is the index of refraction for the anti-reflective coating, and n_{mat} is the index of refraction for the substrate medium. When it strikes the first surface, a small percentage of the light is reflected with a 180° phase shift due to external reflectance. The transmitted light passes through the coating, and strikes the substrate medium where another small percentage of light is reflected with a 180° phase shift, since it too undergoes external reflection. If the distance of the path traversed through the coating is $\lambda/2$, then the light reflected by the

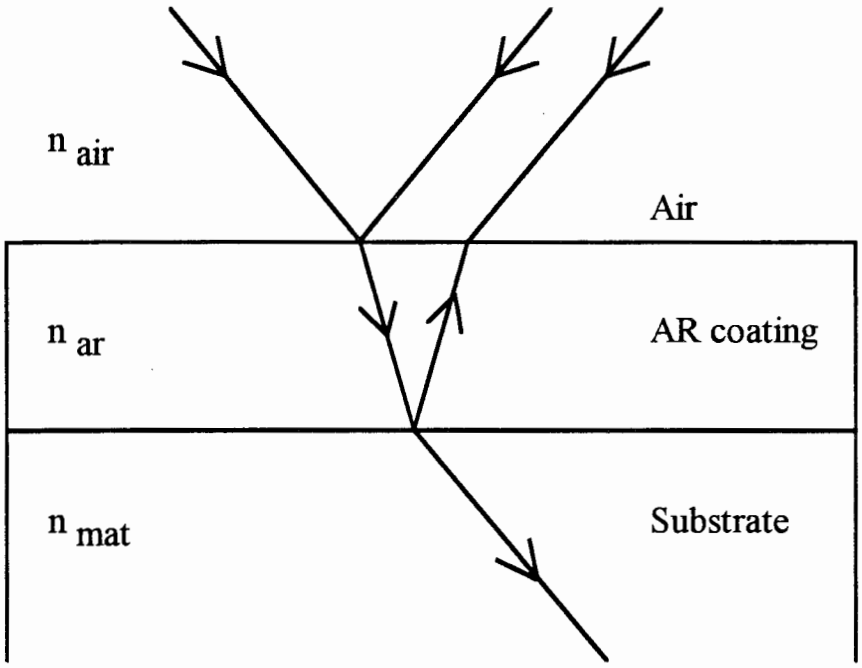

Figure 20. Reflection and transmission from a thin film coating on a substrate..

first interface will cancel the light from the second interface, since the two reflected rays will be 180° out of phase. For simplicity it is assumed that the light incidence is normal to the optical surface, but to separate the two reflected rays, oblique incidence is shown in Figure 20. To obtain perfect cancellation of the reflected waves (maximum transmission), the optical thickness of the anti-reflective coating must be an odd multiple of $\lambda/4$. Because the index of refraction for any material is wavelength dependent, it is

quite clear that coatings are designed for specific wavelengths. Deviations from this wavelength will result in imperfect cancellations and thus poorer transmission.

Through manipulation of Fresnel's equations, the condition for equal magnitude of the reflecting wave fronts off of the two interfaces can be calculated. This condition is met when the air-to-coating index of refraction ratio and the coating-to-air index of refraction ratio are equal,

$$\frac{n_{air}}{n_{ar}} = \frac{n_{ar}}{n_{mat}} . \tag{11}$$

The fact that the incident medium in the above situation is air dictates that the inequality, $n_{air} < n_{ar} < n_{mat}$ is satisfied.

Other factors, besides wavelength dependence, can cause anti-reflective coatings to fail in producing perfect transmission. These include index of refraction of coatings, varying angles of incidence, and curved optics.

A. Index for AR coated optics. Currently there are no durable single layer coatings with indices low enough to meet the requirement of Equation 11. Magnesium fluoride (MgF_2), for example, has an index of 1.38. This coating can create perfect transmission only on optics with an index of refraction of 1.64. This eliminates most common optical materials. In order to compensate for the higher reflectance at the first interface as compared to the lower reflectance at the second interface, multilayer coatings were developed. In the case of a two layer coating the optimal coatings can be describe

by,

$$n_{air} = \frac{n_{ar_1}^{\ 2} n_{mat}}{n_{ar_2}^{\ 2}} \ . \qquad (12)$$

where n_{ar1} is the index of refraction of the top anti-reflection coating and n_{ar2} is the index of refraction of the bottom ant-reflection coating. Multi-layer coatings are also used when coating optics for multiple wavelengths. However, with today's technology it is difficult to produce a coating with a high transmission for more than two wavelengths. The complexity of the equations for layers greater than two interfaces increases exponentially and will not be discussed here.

B. Angle of Incidence. The angle of incidence can have a great impact on the effectiveness of an anti-reflective coating. Thus far normal incidence has been assumed. If light is off normal, the effective ray path length will increase. Since it is wavelength dependant, increasing the path length causes the odd multiples of $\lambda/4$ condition for perfect interference to no longer hold true, and thus transmission will decrease. A second problem with oblique incidence is that, since it is angle dependent, the intensities of reflected light, from the surface of the coating and the material, will differ, and thus not totally cancel.

C. Curved Optics. Curved optics have the same effect on reflectance as does changing the angle of incident of light on a flat surface. However, since the angle of incidence varies over the curved surface, the reflection will vary over the curved surface. This produces non linear effects on the transmitted signal, and can become significant on short focal length lenses. Unless a coating can compensate for the curvature of the surface, the light rays will be reflected as a function of the optical surface curvature and transmitting wavelength.

4.3 Optical Materials

There are a large number of optical materials on the market today. In choosing materials for an optical system, one must consider the properties and cost of each material. In cases where the properties must meet certain design criteria, cost may become less significant. From a list of hundreds, a few of the more commonly used optical materials will be discussed in this chapter. These materials are fused silica (SiO_2), quartz, borosilicate crown glass (BK 7), optical crown glass, pyrex, sapphire, and zinc selenide. Their optical and mechanical properties are summarized at the end of the chapter in Table 3.

A. Fused Silica (SiO_2). Fused silica offers a wide range of applications due to its high degree of purity and transmission spectrum. It transmits more light from the ultraviolet to the infrared than both quartz and glass. Fused silica also has other

advantages over both glass and quartz, such as a low coefficient of thermal expansion. Fused silica can tolerate thermal shock over large temperature transients, and can operate over large temperature ranges. Its structural strength allows fused silica to resists scratching and digging. It also resists darkening from transmitting high-intensity ultraviolet laser energies. Fused silica has very low florescence levels under ultraviolet irradiation, and in some high quality batches it shows no fluorescent response to ultraviolet wavelengths greater than 300 nm.

B. Quartz. Quartz is a naturally occurring substance formed into optical components by crushing the rock and melting it into form. This process allows for imperfections in the material's structure, and thus produces slightly lower ultraviolet transmission than fused silica. Since they are birefringent, quartz crystals are used primarily in the manufacturing of polarizing optics. Quartz also has a very low florescence level, making it suitable for high energy laser systems.

C. Borosilicate Crown Glass (BK 7). From near ultraviolet through near infrared, BK 7 can be the most advantageous optical material. It holds one advantage over all other materials, low cost. Even though it is inexpensive, BK 7 offers a wide range of desirable qualities. It is a hard material and therefore does not scratch easily. It has good transmission down to 350 nm (over 80%). BK 7 is also resistance to chemicals so it is easy to clean.

D. Pyrex. Pyrex is a special type of borosilicate glass that has a spectral range from the ultraviolet to the near infrared. Its structural non uniformity causes the material to have a lower transmission than BK 7, so it should not be used in precision optical designs. Its main advantage is a low coefficient of thermal expansion, making it an excellent material for high temperatures or high temperature gradients. Since it is inexpensive, pyrex is an excellent choice for test plates and windows.

E. Sapphire. Sapphire is one of the strongest and hardest optical materials on the market today. Its strength allows it to be formed into thin optical components, and its hardness resists scratches and chemicals, making it suitable for harsh environments. Because of its high thermal conductivity, windows made from sapphire can be safely heated to keep condensation off, or cooled to dissipate energy caused by high radiation fluxes. Sapphire's spectral range is from 150 nm to 5000 nm. Because of its high index of refraction, sapphire exhibits high external reflectance and thus low transmission. However, this high index of refraction makes sapphire ideally suited for anti-reflective coatings since the coating-to-substrate index of refraction ratio can be matched closely to the air-to-coating index of refraction ratio.

F. Zinc Selenide. Zinc selenide is used mainly in the red and infrared parts of the spectrum. Like sapphire, zinc selenide has a high index of refraction, and must have anti-reflective coatings. Normal transmission for the material is around 70% in its spectral range. Zinc selenide's spectral range allows infrared systems to be aligned using

a simple He-Ne laser (632.8 nm primary wavelength). The material's only drawback is that it is not very hard and must be handled with care.

Table 3. Optical and mechanical properties of some commonly used materials

Property	Fused Silica	Crystalline Quartz	BK 7	Optical Crown Glass	Pyrex	Sapphire	Zinc Selenide
Transmission > 50% (nm)	175 - 3500	165 - 4500	330 - 2600	340 - 2600	300 - 2650	160 - 6000	600 - 12000
Transmission at 1064 nm	94%	93%	92%	90%	90%	86%	70%
Transmission at 532 nm	93%	92%	92%	90%	90%	85%	0%
Transmission at 355 nm	93%	92%	85%	75%	90%	84%	0%
Transmission at 266 nm	92%	92%	0%	0%	10%	80%	0%
Young's Modulus ($10^9 N/m^2$)	73		81	71.5	62.8	345	67.2
Hardness (Knoop) (kg/mm^2)	530	600	520	542	481	1370	120
Density (g/cm^2)	2.202		2.51	2.55	2.23	3.97	5.27
Coefficient of Thermal Expansion ($10^{-7}/°C$)	5.5	5.0	71	93.3	32.5	77	85.6
Thermal Conductivity (W/mK)	1.38		1.114	1.11	1.13	22.2	18.0
Specific Heat (J/gK)	0.743		0.858	0.77	0.76	0.76	0.34
Air-material Surface Reflectance (λ nm) (Refractive index)	3.51% (532) (1.46071)	3.51% (530.9) (1.46098)	4.25% (532) (1.51947)	4.32% (546) (1.52501)	3.7% (546) (1.476)	7.75% (532) (1.7718)	20.1% (589) (2.624)
Birefringent	no		no	no	no	slightly	no

Chapter 5

OPTICAL EFFICIENCIES

In order to calculate the expected signal level of a lidar, the total efficiency of the system must be known. In simple lidar designs which utilize only a few detectors, the total optical efficiency can be measured easily, and may have only minor effects on the signal. This is not the case for the LAMP lidar since its subsystems incorporate a total of 43 optical components. Losses can become intolerable if optics are not properly coated for maximum transmittance and reflectance at each of the wavelengths being monitored. This chapter will discuss the optical efficiencies of the transmitter, receiver, and detector subsystems. The total optical path efficiency has been entered into a model to calculate the expected photon return. The optical transmissions for the beamsplitters, filters, and some of the mirrors were measured with a Cary 5 spectrophotometer. The efficiencies of all other optics were taken from spectral data sheets provided by the manufacturer. These are indicated with an asterisk (*). The system efficiency, $\eta_{eff}(\lambda_s)$, the last factor in the lidar equation (page 8), can be broken up into three components,

$$\eta_{eff} = \eta_T \eta_R \eta_D \ , \tag{13}$$

η_T = Receiver optical efficiency,
η_R = Transmitter optical efficiency,
η_D = Detector optical efficiency.

The receiver and detector optical efficiencies can be determined with relative ease since they have relatively few optical components. The detector system efficiencies, involving 32 components, must account for other effects such as polarization and light vignetting.

5.1 Transmitter System

The transmitter for the LAMP lidar consists of 6 optical components following the Nd-YAG laser: a 5X beam expander (two mirror surfaces), an energy monitor, and four beam steering mirrors. To model the transmitter performance, both the laser power and the optical efficiencies of the beam steering optics must be determined.

A. Energy Measurements. The energy of the laser is measured pulse by pulse using an energy monitor, built at Penn State University, set up directly behind the first beam steering laser hard coated mirror. This mirror only allows 0.36 percent of the laser light to pass through. The energy flux is reduced to such a low level that special hard coated laser optics are not needed for the energy monitor subsystem. After passing through a series of apertures, diffusers, lenses, and filters, each laser pulse is integrated by a high speed photodiode, one for the 532 nm wavelength and another for the 355 nm wavelength. The photodiode signals are sent to the data storage unit and saved in the data files. This type of photodiode is needed because the laser pulses are only 7 ns long. Pulse by pulse measurements ensure that any laser power fluctuations during a data collection run are detected, and the correct integrated power levels are recorded for each

wavelength. The energy monitor is calibrated by splitting off 50% of the laser energy at each of the transmitted wavelengths, feeding half of the energy into a Scientech calorimeter, and allowing the other half to pass through the system. The total 532 nm energy emitted during the thirty minute run used for comparison to the model was measured to be 14701 Joules. Schematic diagrams for the optical section and circuitry of the energy monitor can be found in the Appendix.

B. Optical Efficiencies. Figure 21 is a diagram of the transmitter, showing the optical components encountered by the laser beam. The laser beam is reflected off of three beam steering mirrors and a beam expander. Table 4 provides a summary of the optical efficiencies of the transmitter system components.

Table 4. Summary of transmitter optical efficiencies.

Optic	Optical Efficiency for the Transmitter System (η_T)	
	355 nm	532 nm
2" laser hard coated mirror	0.996425	0.99635
5x beam expander (2 mirrors)	0.9900 *	0.9900 *
4" laser hard coated mirror	0.9976	0.9986
4" laser hard coated mirror	0.9976	0.9986
Total efficiency	0.9817	0.9725

* purchase requirement specification or manufacturer's spectral data sheet

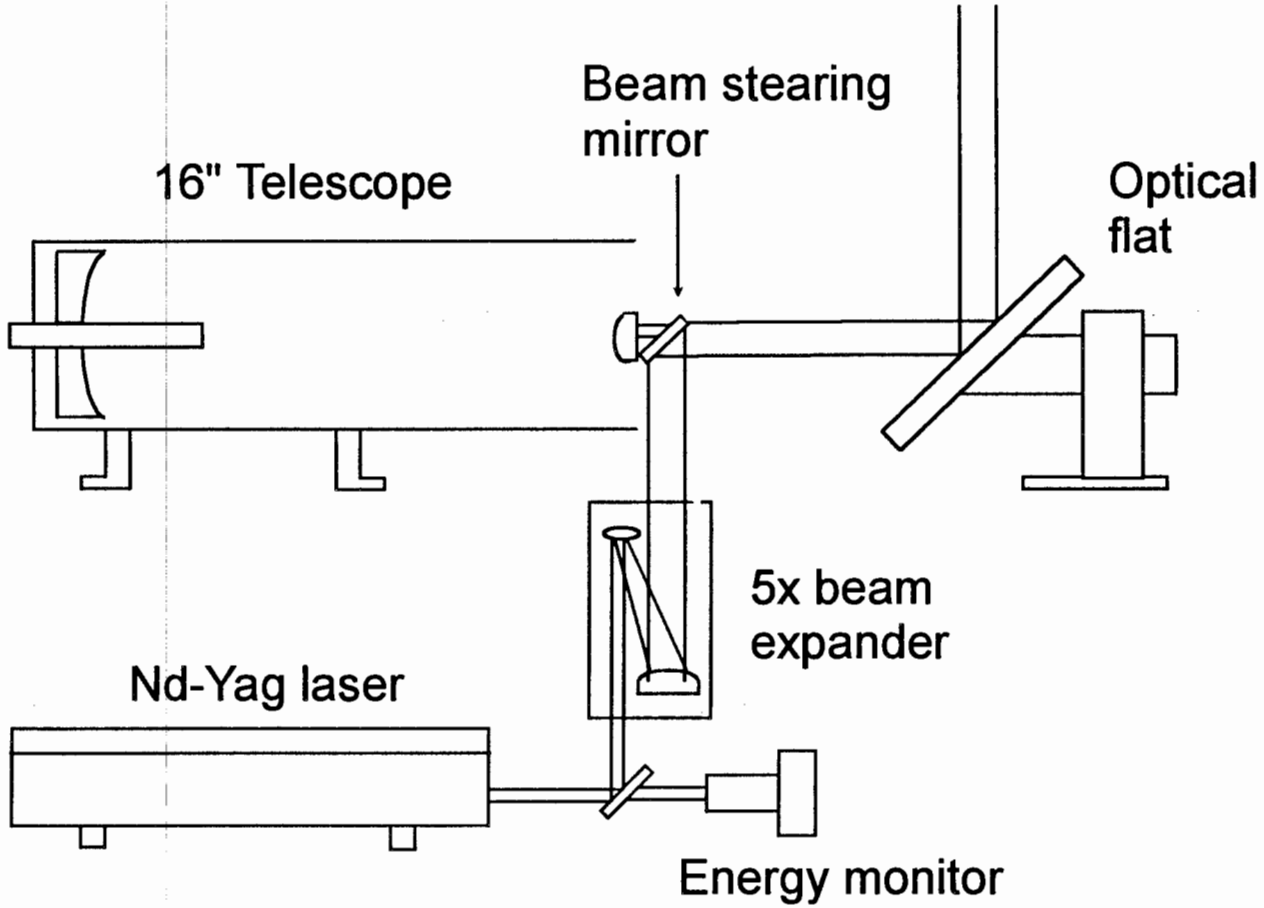

Figure 21. Darwing of the laser beam propagation through the transmitting system. The recieving telescope is included to show where the beam steering mirror is located.

5.2 Receiver System

The receiver system is shown in Figure 10. The returning light encounters seven optical components, two lenses and five mirrors. Both the large flat mirror and the Cassegrain telescope are glass substrates with an aluminum reflective coating and an SiO_2 overcoat. The SiO_2 coating is to prevent oxidation of the aluminum which would lower its reflectivity. SiO_2 has high transmission in the ultraviolet for the 355 nm wavelength.

Table 5. Summary of receiver optical efficiencies.

Optical Surface	Optical Efficiencies for the Receiver System (η_R)			
	355 nm	532 nm	607 nm	660 nm
Optical Flat	0.8950	0.9400	0.9450	0.9400
Telescope	0.9200 *	0.9100 *	0.9050 *	0.9000 *
Beam steering mirror	0.7510	0.8150	0.8037	0.7781
AR coated Fabry lens	0.9950 *	0.9950 *	0.9980 *	0.9975 *
AR coated collimating lens	0.9950 *	0.9950 *	0.9980 *	0.9975 *
Beam steering mirror	0.7510	0.8150	0.8037	0.7781
Total efficiency	0.4598	0.5625	0.5502	0.5096

* purchase requirement specification or manufacturer's spectral data sheet

5.3 Detector System

The detector system accounts for the bulk of the optical components in the LAMP lidar system (32 out of 43 components). The primary detector box houses six separate data channels which monitor the wavelengths 355 nm, 532 nm, 607 nm, and 660 nm. Because of the large number of components, the optical efficiency, η_D, for the detector box can be broken up into four separate parts,

$$\eta_D = \eta_O \eta_{PH} \eta_{THR} \eta_P \,, \tag{14}$$

η_O = optical efficiency,
η_{PH} = photomultiplier quantum efficiency,
η_{THR} = vignetting,
η_P = polarization efficiency.

The optical efficiency and PMT quantum efficiency components, can be measured accurately. Deviations from this quantity can occur due to environmental effects on coatings and materials, dust, and PMT dynode degradation. Light vignetting and polarization effects can change slightly from one measurement to the next, depending on the exact beam alignment and the degree of polarization in the backscattered signal. A schematic diagram of the detector box with all of its optical components is provided in Figure 22. Tables 6, 7, and 8 give the efficiency of each component in the different detector paths, with the identifying numbers in Figure 22 (page 55) and its key (pages 56 and 57).

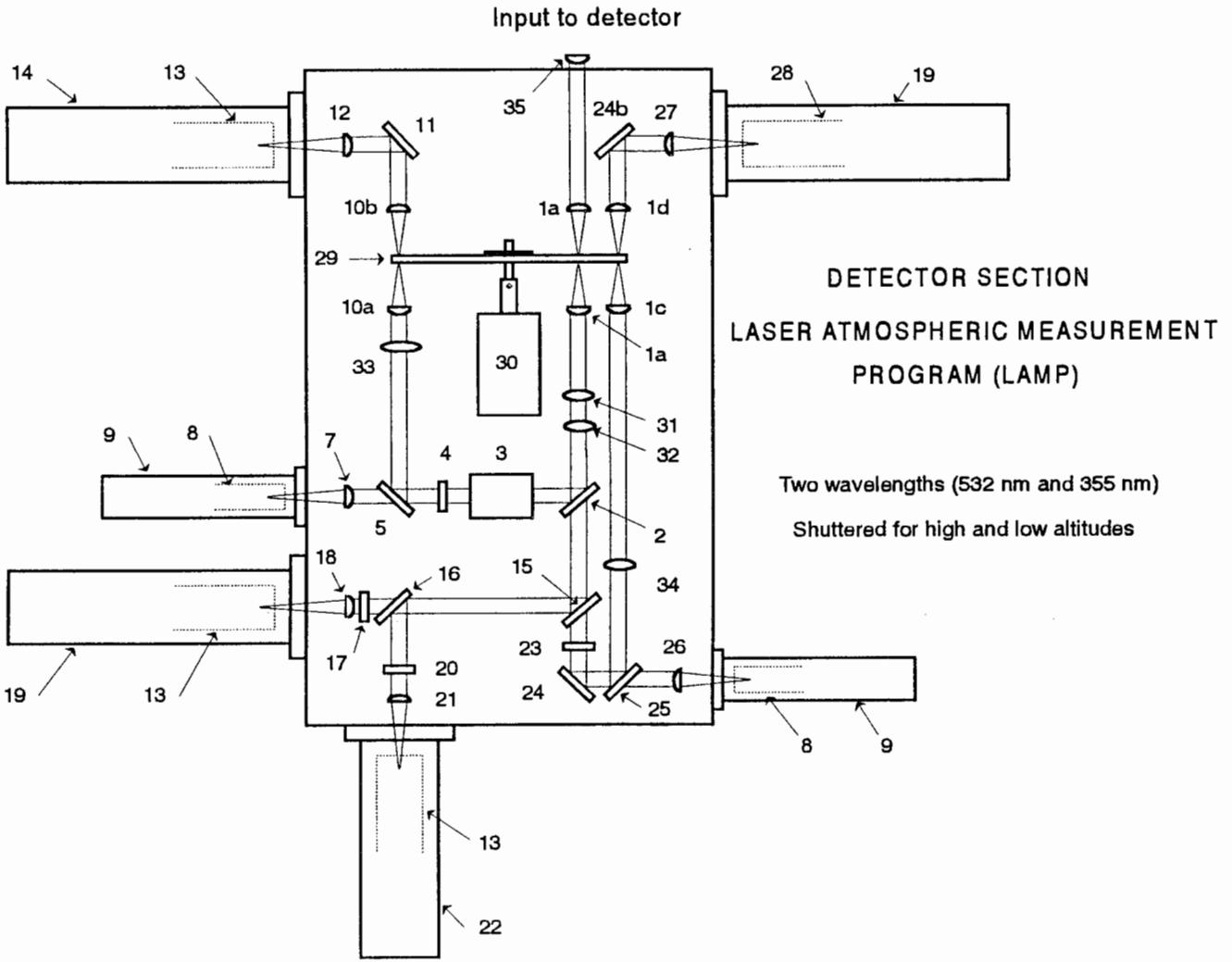

Figure 22. Schematic drawing of the detector section for the LAMP lidar [21].

Key to Figure 22

1a-d) Fused silica plano-convex lens, d = 25.4 mm, F = 50.8 mm, AR coated for 355, 532, 607,and 660 nm.

2) Dichroic beam-spitter, d = 50.8 mm, splits off 532 nm from 355, 607 and 660 nm.

3) Fabry-Perot etalon, electronically tuned to transmit 532 nm with a 0.01 nm. bandwidth.

4) 532 nm narrow band-pass filter with a 0.29 nm bandwidth, temperature stabilized at 34° C.

5) 532 nm beam-spitter.

7) Glass plano-convex lens, d = 25.4 mm, F = 175 mm, AR coated for 532 nm.

8) 28 mm Thorn EMI 9828B03 PMT, analog data which is digitized, (2 ea.).

9) 28 mm Thorn EMI socket and housing assembly.

10a-b) Glass plano-convex lens, d = 25.4 mm, F = 50.8 mm, AR coated for 532 nm.

11) 532 nm high reflectivity mirror, d = 50.8 mm.

12) Glass plano-convex lens, d = 25.4 mm, F = 200 mm, AR coated for 532 nm.

13) 52 mm Thorn EMI 9863B/350 PMT, photon counting, (2 ea.).

14) 52 mm Thorn EMI thermoelectric cooled (-25° C) PMT socket and housing .

15) Dichroic beam-spitter, d = 50.8 mm, splits off 355 nm from 607 and 660 nm.

16) Dichroic beam-spitter, d = 50.8 mm, splits off 607 nm from 660 nm.

17) 607 nm band-pass filter, with a 3.5 nm bandwidth.

18) Glass plano-convex lens, d = 25.4 mm, F = 62.9 mm, AR coated for 607 nm.

19) Amherst Scientific thermoelectric cooled (-30° C) PMT socket and housing .

20) 660 nm bandpass filter, with a 3.5 nm bandwidth.

21) Glass plano-convex lens, d = 25.4 mm, F = 200 mm, AR coated for 660 nm.

22) Pacific Research thermoelectric cooled (-25° C) PMT socket and housing.

23) 355 nm bandpass filter, with a 3.2 nm bandwidth.

24a-b) 355 nm high reflectivity mirror, d =50.8 mm.

25) 355 nm beamsplitter.

26) Fused silica plano-convex lens, d = 25.4 mm, F = 175 mm, AR coated for 355 nm.

27) Fused silica plano-convex lens, d = 25.4 mm, F = 100 mm, AR coated for 355 nm.

28) 52 mm Thorn EMI 9893B/350 PMT, photon counting.

29) Aluminum high speed (4800 rpm) optical chopper wheel, d = 10 inches.

30) Hysteresis synchronous motor for the chopper wheel.

31) General purpose optical mirror, d = 50.8 mm.

32) General purpose optical mirror, d = 50.8 mm.

33) Glass plano-convex lens, d = 50.8 mm.

34) Glass plano-convex lens, d = 50.8 mm.

Table 6. Summary of detector optical efficiencies for the 355 nm channels in the low and high altitudes.

Optic #	Optical Efficiencies for the Detector System (η_o)	
	355 nm low altitude	355 nm high altitude
35	0.9950 *	0.9950 *
1a	0.9950 *	0.9950 *
1b	0.9950 *	0.9950 *
31	0.7510	0.7510
32	0.7510	0.7510
2	0.8361	0.8361
15	0.8065	0.8065
23	0.2166	0.2166
24	0.9989	0.9989
25	0.0065	0.9935
26	0.9950 *	
34		0.9200 *
1c		0.9950 *
1d		0.9950 *
24b		0.9989
27		0.9950 *
Total efficiency	0.000524	0.0729

* required purchase specification or manufacturer's spectral data sheet

Table 7. Summary of detector optical efficiencies for the 532 nm channels in the low and high altitudes.

Optic #	Optical Efficiencies for the Detector System (η_o)	
	532 nm low altitude	532 nm high altitude
35	0.9950 *	0.9950 *
1a	0.9950 *	0.9950 *
1b	0.9950 *	0.9950 *
31	0.8150	0.8150
32	0.8150	0.8150
2	0.9991	0.9991
4	0.5500 *	0.5500 *
5	0.0064	0.9936
7	0.9950 *	
33		0.9200 *
10a		0.9950 *
10b		0.9950 *
11		0.9992
12		0.9950 *
Total efficiency	0.00229	0.3235

* purchase requirement specification or manufacturer's spectral data sheet

Table 8. Summary of detector optical efficiencies for the 607 nm and 660 nm channels.

Optic #	Optical Efficiencies for the Detector System (η_o)	
	607 nm nitrogen	660 nm water vapor
35	0.9800 *	0.9750 *
1a	0.9800 *	0.9750 *
1b	0.9800 *	0.9750 *
31	0.8037	0.7781
32	0.8037	0.7781
2	0.7817	0.9010
15	0.9969	0.8381
16	0.7634	0.9938
17	0.8288	
18	0.9800 *	
20		0.8113
21		0.9750 *
Total efficiency	0.2938	0.3331

* purchase requirement specification or manufacturer's spectral data sheet

A. Photomultiplier Tubes The received light is processed by the optics in the detector box into the four monochromatic components of 355 nm, 532 nm, 607 nm, and 660 nm wavelengths. These components are fed to photomultiplier tubes, where the light is converted into electrical signals. Photons striking the photocathode eject electrons which are sent through a series of dynodes to multiply the initial photoelectrons by 6 to 7 orders of magnitude. At the end of the dynode chain, the anode collects the electrons to produce a signal to be monitored by more electronics.

The most important characteristic in all photomultiplier tubes is the quantum efficiency of the photocathode. Quantum efficiency can be defined as the probability that a photon will be detected by the photocathod at a specific wavelength. Typically, photocathodes have larger quantum efficiencies in the ultraviolet than in the visible or infrared regions of the spectrum. Since most PMT's do not reach quantum efficiencies much greater than 25%, great care must be taken in choosing a proper tube for the signal to be measured. The quantum efficiencies for the PMT's of the LAMP lidar are shown in Table 9.

Because the levels of light received in the high altitude and Raman channels are so low, photon counting PMT's with fast response times were chosen. The high intensity light returning from the lower altitudes dictated digitization of analog current signal measurements.

Table 9. Photomultiplier quantum efficiencies for the LAMP optical detector channels

Photomultiplier Type	Photomultiplier Tube Quantum Efficiencies			
	355 nm	532 nm	607 nm	660 nm
THORN EMI #9828 Analog photomultiplier	14% Low Altitude	10.5% Low Altitude		
THORN EMI #9893B/350 Photon counter	21.8% High Altitude			
THORN EMI #9863B/350 Photon counter		11% High Altitude	6%	2%

Dark current, saturation, dynode degradation, and pulse overlapping, can cause errors in the monitored PMT signal. Dark current is caused by the release of electrons in the absence of illuminating light on the photocathode. If the dark current is high in the presence of a low light signal, the signal-to-noise ratio will be low. The main cause for dark current is thermal release of electrons from the photocathode. For this reason, the photon counting PMT's are thermoelectrically cooled. Cooling is not necessary for the low altitude analog PMT's because the signal level is so high. Cosmic rays and other background radiation also release electrons that contribute to the dark current..

PMT saturation occurs when the photocathode is struck by too large a concentration of photons, causing the photocathode to release a large cloud of electrons down the dynode chain. If the concentration of electrons is too large, the last dynodes will experience a drop in voltage because their current is so large. This voltage drop will

decrease the number of electrons released at the next surface, thereby causing a nonlinear effect in the received electron signal. Saturation continues to occur until the dynode can reestablish its original voltage. Because the recharging time constant is large compared to that for a normal charge pulse, the response may be non-linear for a fraction of a second. To avoid saturation in the LAMP system, a shutter wheel shields the high altitude photon counters from the high intensity low altitude light.

Dynode degradation (drift) is caused by the effects of saturation and time. Since it can not keep up with high concentrations of electrons, the surface of a saturated dynode will begin to degrade. Similarly, long periods of use will slowly degrade the surface of the dynode. These effects can reduce the gain of the current received at the anode, reducing the signal-to-noise ratio. It has been assumed that these effects have been minimal in the LAMP lidar. The quantum efficiencies are taken as those given by the manufacturer.

Pulse overlap occurs when a pulse generated by photons blends with another pulse, making discrimination between the two pulses impossible. This effect is only important in photon counting PMT's, since in analog PMT's, the output signal is a current as opposed to discriminated pulses. Pulse overlap can occur in three places: PMT's, discriminators, and the data collection unit. If two photons strike it simultaneously, a photocathode will blend the response as one large pulse. If the discriminator's pulse width is slower than the speed at which photons strike the PMT, than consecutive pulses may be blended into one pulse. Finally, if the data storage unit is not fast enough to respond to the speed of the PMT's and discriminators, pulses may not be counted.

B. Detector Box Vignetting. Because of optical aberrations, perfect collimation of a light beam is impossible. As the optical path length and the number of optical components increases, so does the probability that some of the light will be blocked. The amount of blocked light can be altered if the optical path is shifted from its original position. The further a component is from the detector, the larger the effect on vignetting an optical component can have if it shifted in its location. To reduce light attenuation, rigid structures must be used to avoid misalignment due to vibrations.

C. Polarization. The Fresnel equations show that a surface will reflect the different components of polarization with different efficiencies. In an optical system with a large number of reflecting surfaces, polarization can be a significant problem. Since molecular scattering preserves the polarization of a light source, the polarization axis of the detector box could be oriented to match that of the incoming signal. However, the lower atmosphere contains a large number of aerosol scatterers which tend to depolarize light. This will cause an attenuation in the detected signal because the detector box's polarization orientation will filter out some of this light. As the number of aerosol scatterers fluctuates so does the amount of depolarization.

Though they can be significant, the vignetting and polarization of the detector box were not able to be measured for inclusion into the performance analysis, and thus will be set equal to unity for the photon return model. However, through preliminary measurements, it is estimated that the attenuation factor due to polarization is of the order of two. Future measurements will be performed to obtain an exact value.

5.4 Total Optical Efficiency

Table 10 lists the total optical efficiencies for the LAMP lidar system.

Table 10. Total optical efficiencies for the LAMP measuring channels.

	Optical Efficiencies					
	355 nm Low Alt.	355 nm High Alt.	532 nm Low Alt.	532 nm High Alt.	607 nm	660 nm
Transmitter	0.9817	0.9817	0.9725	0.9725	0.9725	0.9725
Receiver	0.4598	0.4598	0.5625	0.5625	0.5502	0.5096
Detector Optics	0.000524	0.0729	0.00229	0.3235	0.2938	0.3331
PMT's	0.14	0.218	0.105	0.11	0.06	0.02
Total Efficiency (10^{-5})	3.311	717.0	13.19	1946.6	943.2	328.1

Chapter 6

MODEL DEVELOPMENT AND DATA COMPARISON

A comparison between measured data and modeled expected photon return data has been performed to asses the operating characteristics of the LAMP lidar. The model is based on the lidar equation (Chapter 2), and the LAMP efficiency factors (Chapters 3 and 5). This chapter will summarize the factors that went into the expected photon return model, and analyze any deviations from measured lidar data. Areas for improvement to the model will also be discussed at the end of this chapter. The analysis was performed on the high and low altitude 532 nm channels and on the nitrogen (N_2) channel. Because of the variability of H_2O concentrations in the troposphere, model data has not been calculated for the LAMP water vapor channel. Since the high altitude data is affected by the low altitude meteorological conditions, as discussed in Chapter 2, the comparison between measured and modeled data will begin in the low altitudes and move up to the high altitudes.

6.1 Model Parameters

The backscatter coefficient for the 532 nm wavelength was calculated by Equation 2 in Chapter 2, while the backscatter coefficient for the 607 nm wavelength was found in Laser Remote Sensing [9]. The telescope probability factor was calculated using the computer program discussed in Chapter 3. Atmospheric transmission was calculated using

the LOWTRAN 7, and density was derived from the U.S. Standard Atmosphere, 1976 model. The parameters used in the model calculations are summarized in Table 11.

Table 11. Parameters used in the expected photon return model for the LAMP lidar system

Model Parameter	532 nm Low Altitude	532 nm High Altitude	607 nm Nitrogen	660 nm Water vapor
Backscatter coefficient (10^{-28}cm^2/sr)	6.2259	6.2259	0.00564	0.1257
Integration altitude (m)	15 m	75 m	75 m	75 m
LAMP optical efficiency (10^{-5})	13.19	1946.6	943.2	328.1
Laser energy	14701 Joules (36000 laser shots)			
Transmitted wavelength	5.32×10^{-7} m			
Plank's constant	6.626×10^{-34} J -sec			
Speed of light	2.9979×10^{8} m/sec			
Area of objective mirror	0.1297 m^2			
Receiver probability	Telescope probability model			
Atmospheric number density	U.S. Standard Atmosphere, 1976			
Atmospheric transmission	LOWTRAN 7			

A. U.S. Standard Atmosphere, 1976 (USSA76). The U.S. Standard Atmosphere, 1976 is an idealized, steady-state representation of mean annual conditions of the Earth's atmosphere from the surface to 1000 km at Latitude 45° N, as it is assumed to exist during a period with moderate solar activity [3]. The profiles of atmospheric properties for the USSA76 were obtained through measurements taken from various meteorological balloons and rockets, as well as, scientific research rocket payloads and low Earth orbit satellites. Because this model is based on profiles representing the average conditions for a particular latitude and solar activity, it is not a perfectly description of the atmosphere at the time of the measurements, but should describe conditions of the long term global mean. Figure 23 shows a plot of the atmospheric number density from the USSA76 model [24]. The nitrogen number density was calculated by multiplying the USSA76 model by 0.78, which is the nitrogen percent concentration of the dry atmosphere.

B. LOWTRAN 7. The atmospheric transmission for the model comparison was calculated using the LOWTRAN 7 model [18]. The LOWTRAN model was developed to provide a fairly accurate, simple and rapid means of estimating the transmittance and background radiance of the Earth's atmosphere at moderate resolution (20 cm^{-1}) over a broad spectral interval (350 to 40000 cm^{-1}) [3]. Transmission, calculated for the wavelengths 355 nm, 532 nm, 607 nm, and 660 nm from the ground to 100 km, is shown in Figure 24. Because the backscattering cross section is proportional to λ^{-4}, ultraviolet light is scattered more strongly than visible or infrared.

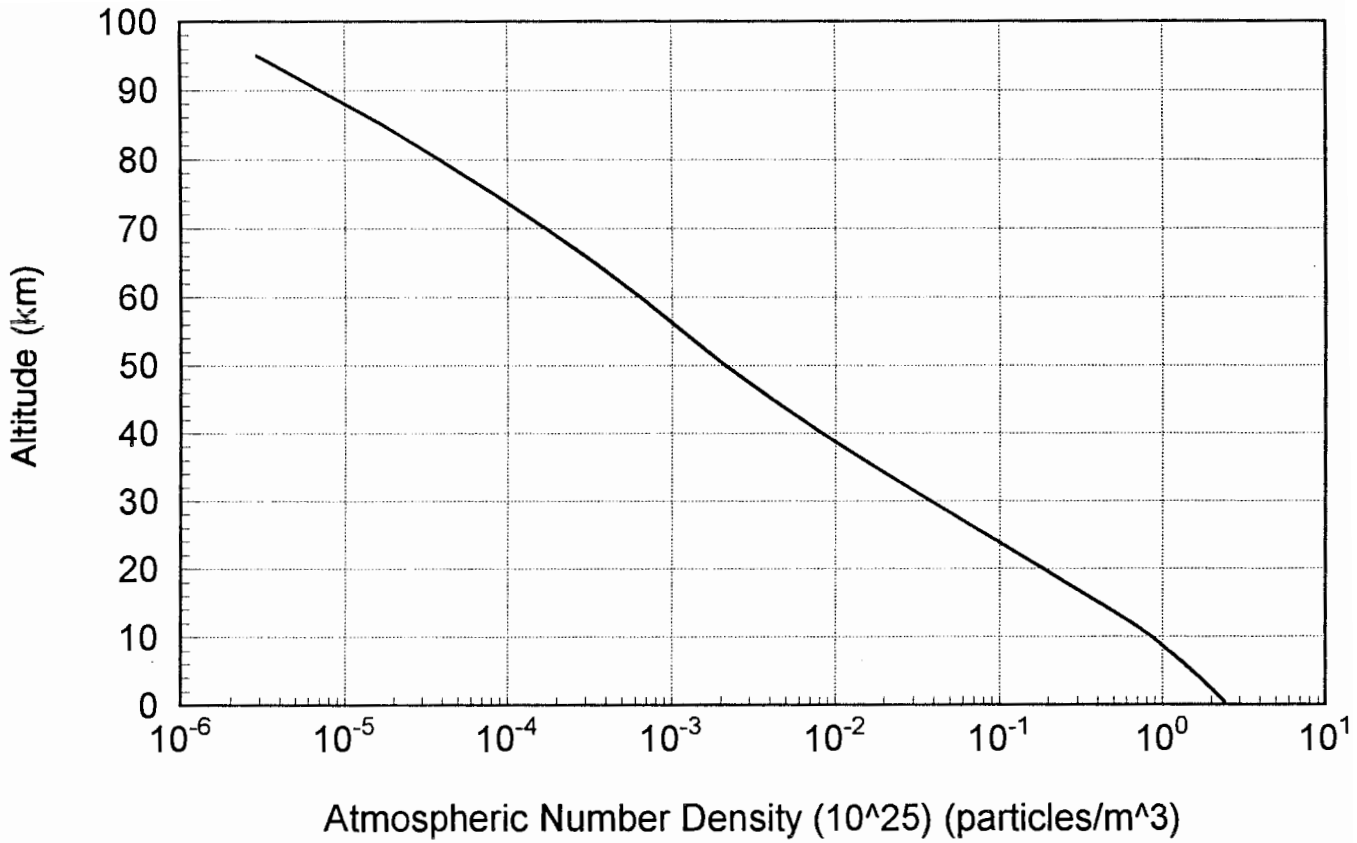

Figure 23. U.S. Standard Atmospher, 1976 model number density used for the expected photon return model.

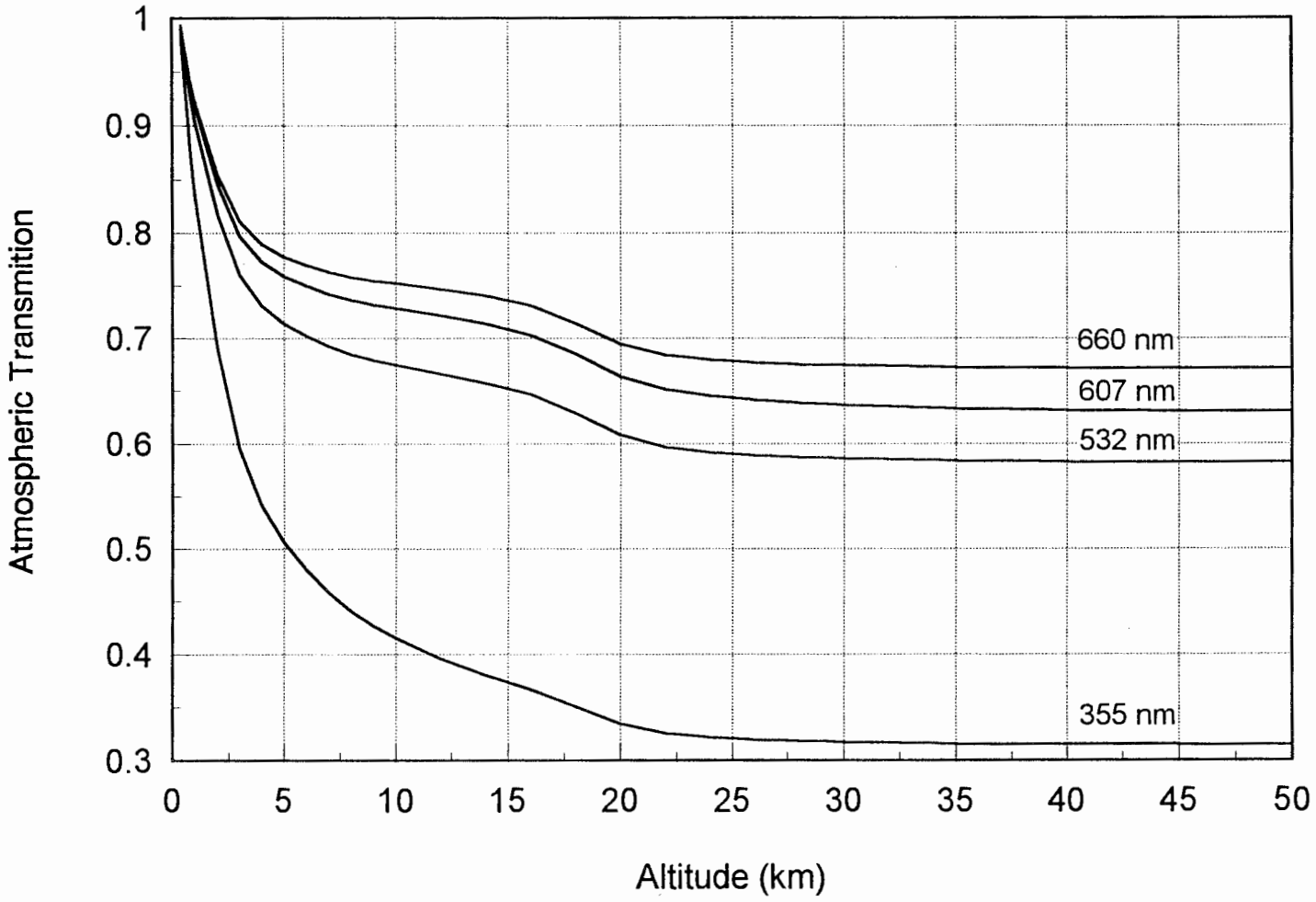

Figure 24 LOWTRAN 7 atmospheric transmission profiles for the LAMP lidar's detected wavelengths, 355 nm, 532 nm, 607 nm, and 660 nm.

Therefore, there is lower transmission for the 355 nm wavelength than for the 532 nm, 607 nm, and 660 nm wavelengths. Table 12 lists the parameters used to calculate the atmospheric transmissions for each of the wavelengths. It is quite evident that there will be errors in the estimated transmission because the model cannot exactly represent the meteorological conditions at the time of measurement. Also, there are unknown absorptions by varying concentrations of atmospheric components, such as ozone, at various altitudes.

Table 12. Atmospheric model parameters used in LOWTRAN 7.

Atmospheric Model Parameter	**Atmospheric Condition**
Model type	Midlatitude summer
Scattering type	Without multiple scattering
Surface albedo	Albedo = 0.3
Extinction type for boundary layer	RURAL extinction
Visibility	Default visibility = 23 km
Stratospheric aerosols	High volcanic profile and aged volcanic extinction
Cloud coverage	None
Starting altitude with respect to sea level	Altitude = 0.354

6.2 Data Comparison

Data from the 532 nm and 607 nm LAMP data channels, obtained on the night of 15 September, 1992, were used for comparison to the model of the expected photon return. The parameters used in the model calculations represent the operating conditions at the time of measurement. To further account for the differences between the modeled and measured profiles, data obtained under similar operating and meteorological conditions on 4 April, 1992, were included in the plots. In either case of data profiles, deviations due to receiver probability, optical efficiencies, and atmospheric number density will be of minor concern. The field of view and alignment of the telescope were checked before each data set run. Optical efficiencies were accurately measured using either a Cary 5 spectrophotometer or the manufactures' spectral data sheets. Finally, the atmospheric number density does not strongly deviate from normal, except during atmospheric anomalies, such as, stratospheric warmings, which can cause deviations of more than a factor of two.

Other factors, such as, polarization and vignetting of the detector box, depolarization due to particle scattering, and atmospheric transmission will cause deviations from the model. The attenuation of the signal due to polarization of the detector box can cause sensitivity variations of as much as a factor of two from the normal signal. Since this factor is caused by the positioning and orientation of the optical components, it should remain a constant factor. The effective sensitivity will vary only with a changing degree of polarization of the light returning from the atmosphere. The

larger the number of particles in the atmosphere, the larger the amount of depolarization in the backscattered light.

Between the time of measurements for each of the data sets, adjustments to the detector box have been made. Since some of the detector paths are intertwined with others, due to the mechanical arrangement of the detector box, these adjustments may have resulted in either a positive or negative effect in the returning signal. Thus improvements in one channel may cause an increase in vignetting in the other channel.

The variability in atmospheric transmission may cause large deviations from the expected photon return. Strong haze or clouds can significantly reduce or eliminate the transmitted and returning signal. Though they are minor, clouds in the April data set have caused the detected signal to be attenuated.

A. 532 nm Low Altitude. It is difficult to do a comparison between measured and calculated profiles in the lower altitudes because of the strong signal due to aerosol contamination in the troposphere. Figures 25 and 26 show profiles for the lower atmosphere for different altitude ranges. The troposphere backscatter intensity is drastically different for each range. Near field effects of overfilling of the telescope focal plane begin to be significant below 1 km. Figure 25 shows the entire range for the low altitude channel while Figure 26 only shows the first three kilometers and emphasizes the region where the boundary layer exists. The boundary layer is the portion of the atmosphere which contains the highest concentration of aerosols, both natural and man-made, and is highly variable as seen by the jump in photon counts below 2.2 km.

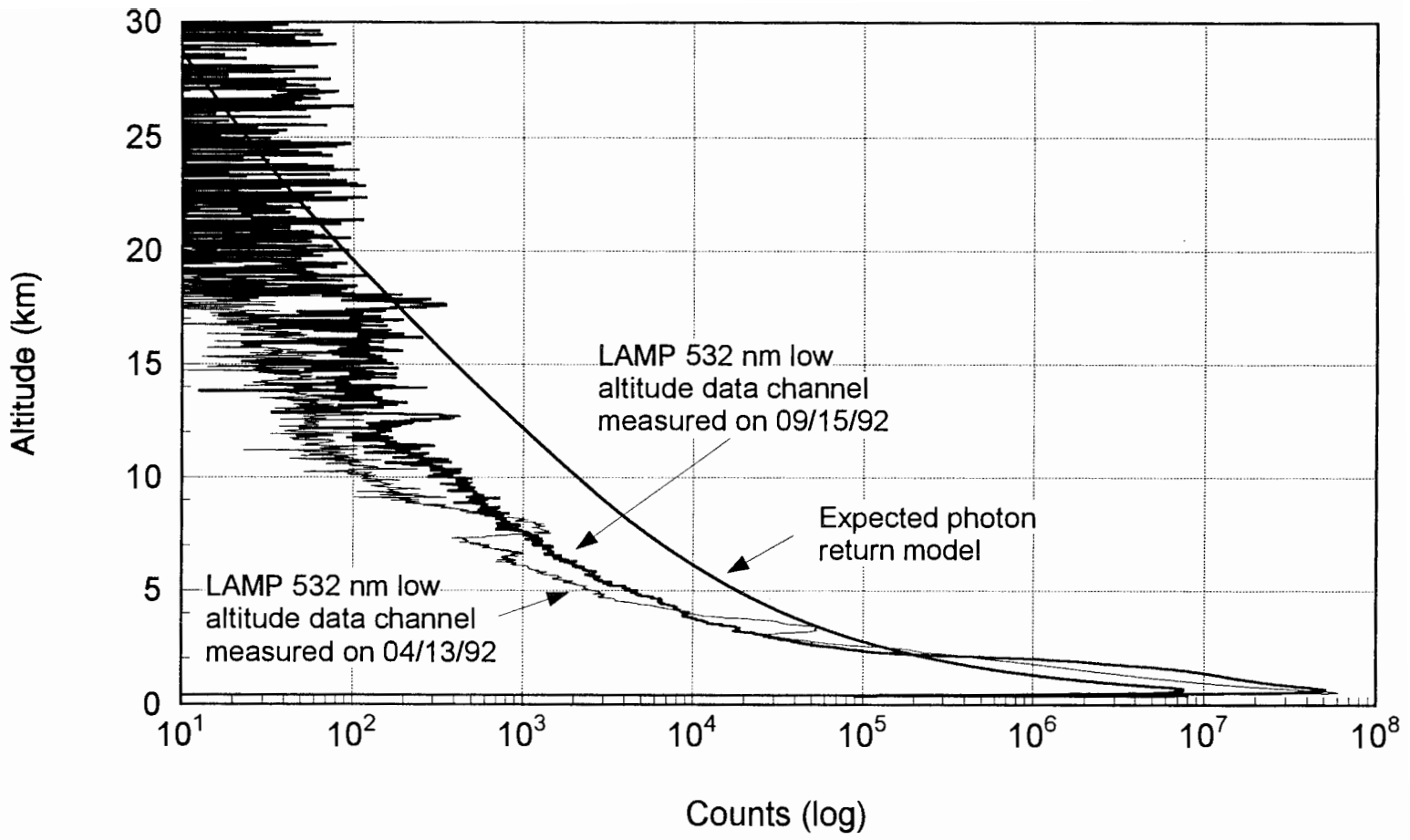

Figure 25 Comparison of the expected photon return and 532 nm low altitude data measured on 04/13/92 and 09/15/92.

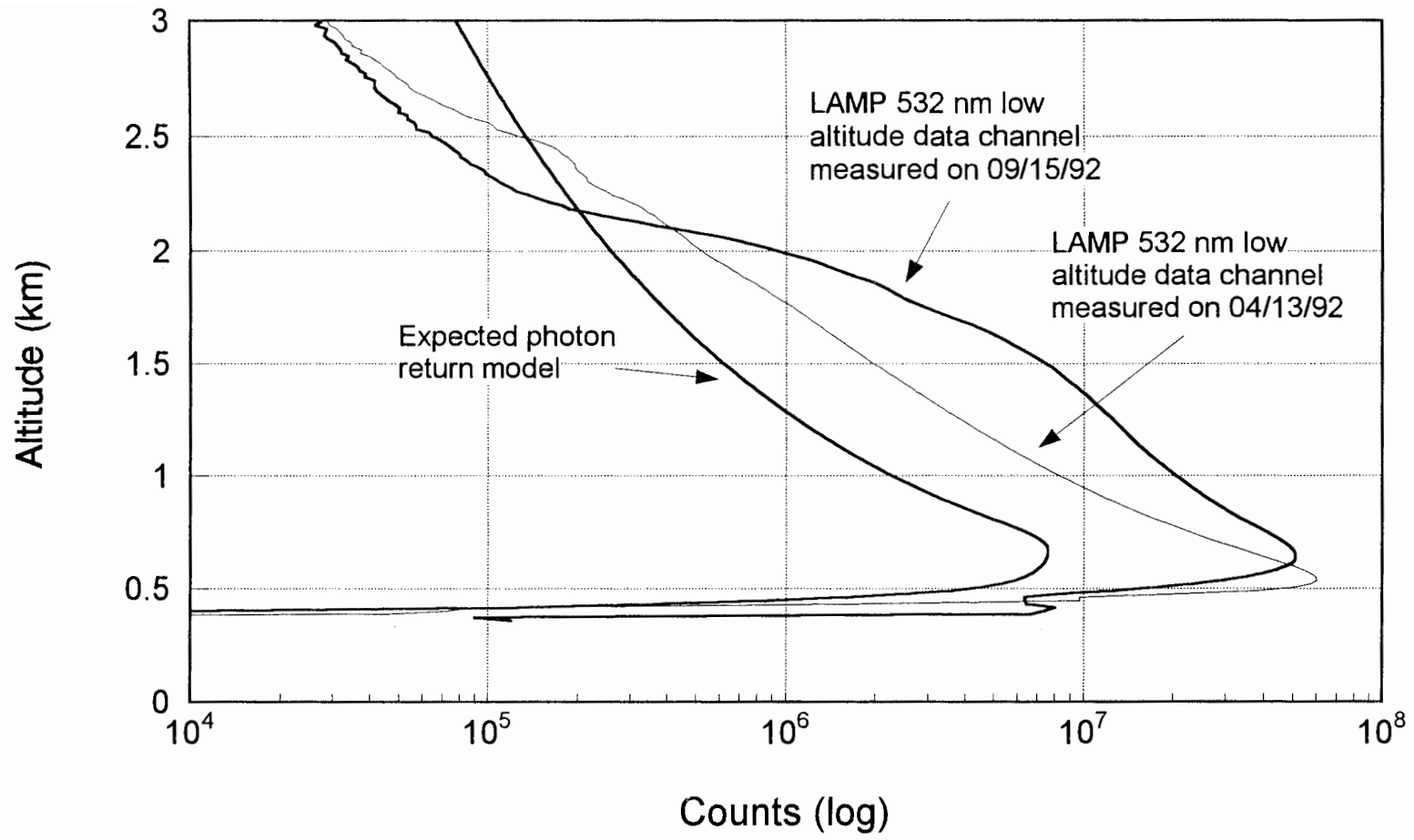

Figure 26. Comparison of the expected photon return and 532 nm low altitude data below 3 km, measured on 04/13/92 and 09/15/92.

Deviations from the model profile are caused by extinction from aerosol scattering, detector box misalignment, and polarization. Data measured in September showed larger aerosol scattering in the boundary layer below 2 km than in April. The April data set showed larger aerosol scattering in the upper troposphere, clouds at 3.5 km and 7 km, than the September data set. Even though LOWTRAN 7 takes into account aerosol scattering in the troposphere, the signal from both days falls below the model after approximately 2.2 km. Also, the signal drops off more quickly in April, after the cloud layers, than in September without the cloud layers. This is typical of attenuation of the transmitted and returning signal due to extinction. Since the cloud layers are small, this extinction will only decrease the detected signals from the high altitudes by small amounts.

The effects of telescope vignetting can be seen in Figure 26. It is important to note that data were taken in April with a much larger field stop than that used in September. Thus, the telescope opened up completely at 550 meters in April and at approximately 700 meters in September. The opening of the telescope for the September data set matches closely with it, since the model was calculated with the field stop aperture used in September.

B. 532 nm High Altitude Channel. Figure 27 presents the results from the model and two measurement sessions for the 532 nm high altitude channel. Since the LOWTRAN 7 model cannot accurately describe the stratospheric aerosol layer, comparisons of the model to actual measurements at the higher altitudes can only be

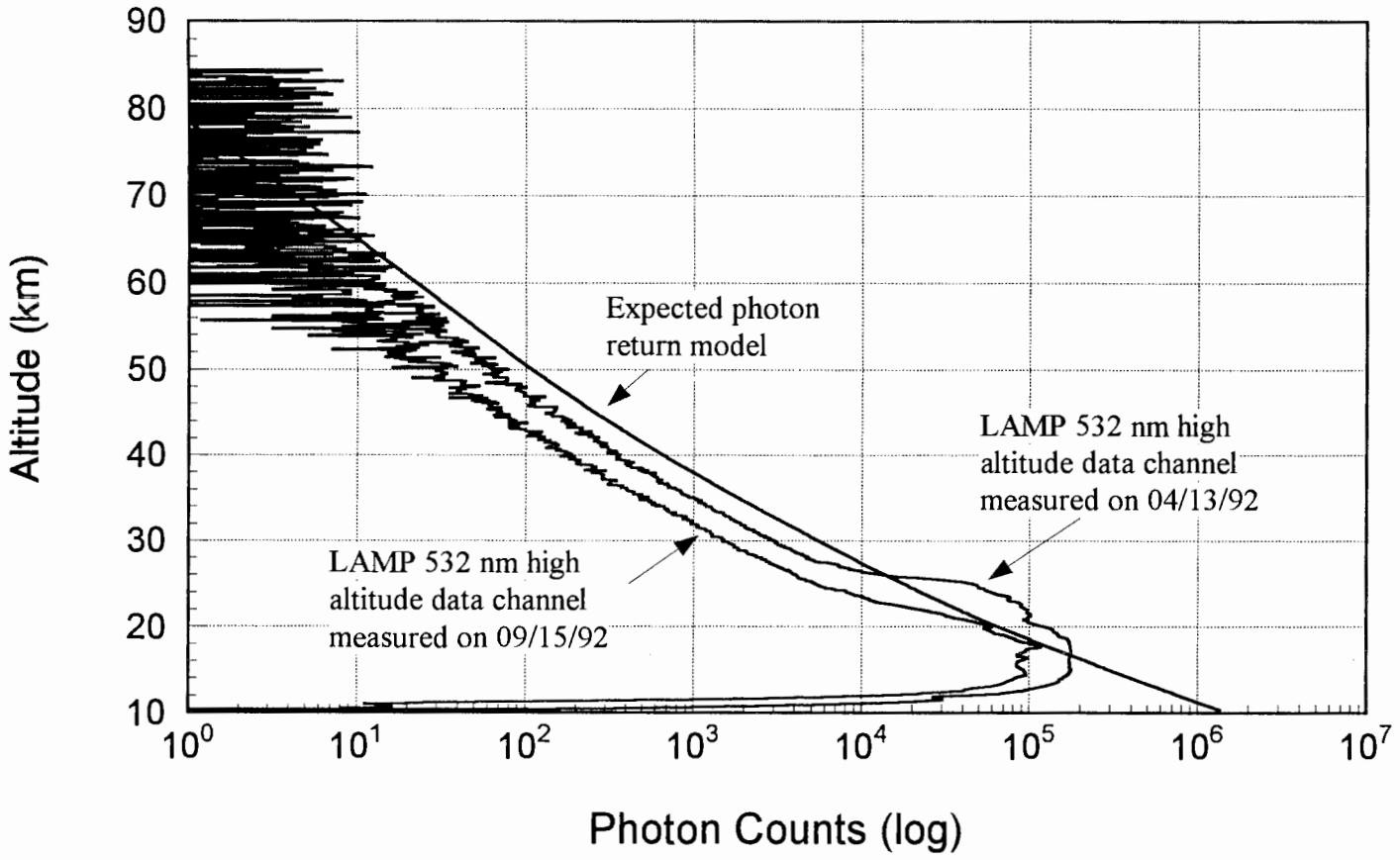

Figure 27. Comparison of the expected photon return and 532 nm high altitude measured on 04/13/92 and 09/15/92.

obtained where the layer ceases to exist, in these cases above 27 km. LOWTRAN 7 fails to describe the stratospheric aerosol layer because, as seen from the two measured profiles, the aerosol layer can change dramatically in size, shape, and content over time periods of weeks at the same geographical location. In both cases, the measured profiles are shuttered out below 19 km to protect the PMT's from the high intensity light returning from the lower altitudes. The curvature of the signal below 19 km results from opening of the mechanical shutter wheel [21].

After accounting for factors, such as, extinction due to the lower atmosphere and stratosphere, and attenuation due to detector box polarization, the high altitude data profiles still show a difference from the expected photon return. The primary remaining factor is the alignment and vignetting of the signal as it passes through the detector box. It was later found that the detector box components, on the 532 nm high altitude channel were slightly misaligned during August 1992. Had this channel been properly aligned, the April high altitude profile would have shown a lower signal count than September, since it experienced greater extinction in the troposphere and stratosphere.

C. 607 nm Nitrogen Channel. The upper ends of the high altitude channels are good indicators of performance, because of the negligible effects due to aerosols. Similarly, the nitrogen channel is a good indicator of low altitude performance, since it too is unaffected by aerosols, except for extinction. This can clearly be seen in Figure 28 for the April profile where the cloud layers exists. The nitrogen profile shows no sign of significant signal enhancement. Though they are important, attenuation due to

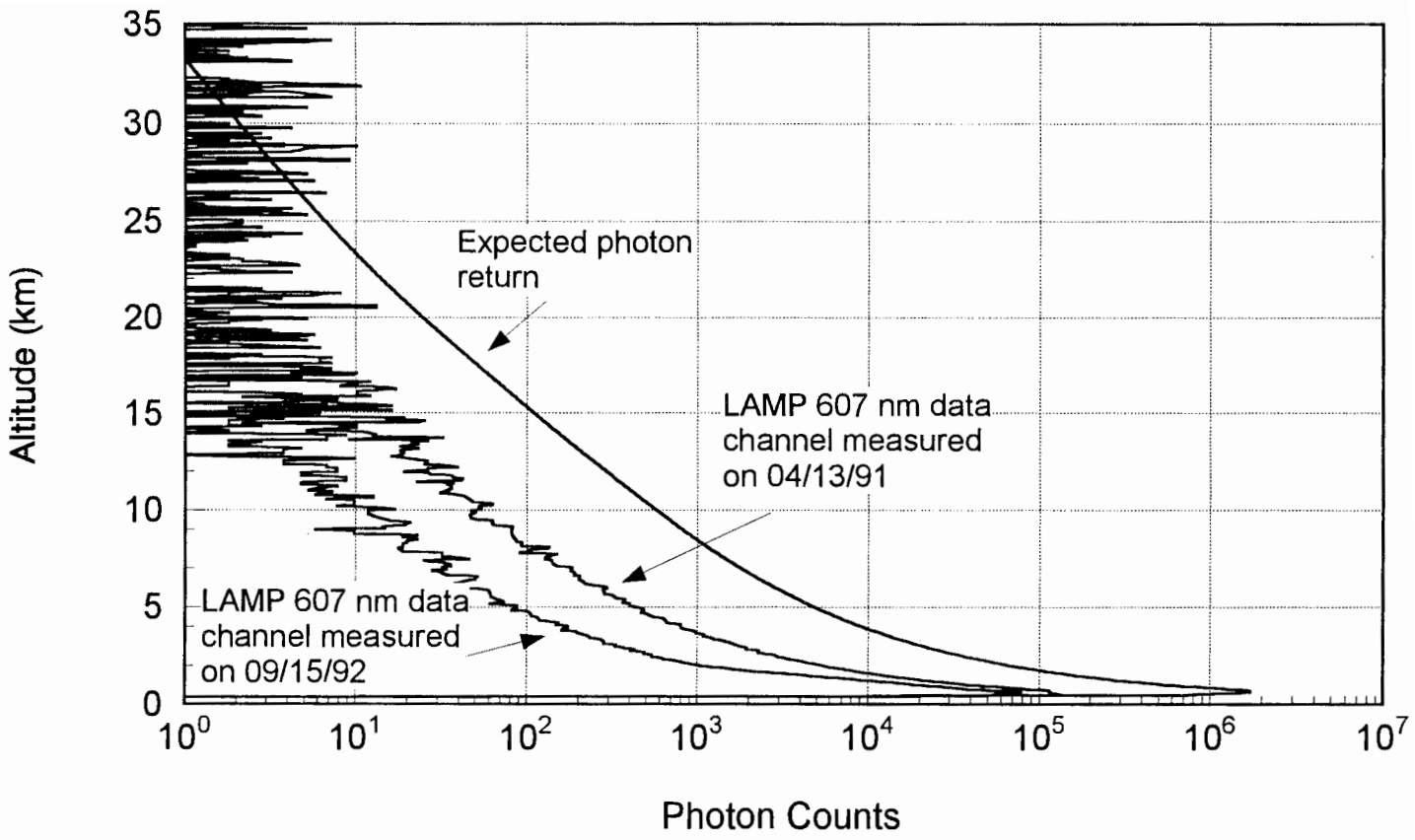

Figure 28. Comparison of the expected photon return and 607 nm nitrogen data measured on 04/13/92 and 09/15/92.

polarization and atmospheric transmission can not totally account for the large deviations shown in both the April and September data. It was shown in Figure 6 of Chapter 2, that in order to cause a decrease from normal in the nitrogen profile of one order of magnitude, an aerosol layer must show 2.5 orders of magnitude enhancement in the 532 nm wavelength over a layer thickness greater than 4 km. This kind of layer is not in either the April or September data set. Also, in both April and September, the signal is initially at least one order of magnitude lower than the model profile. This can only be accounted by the effects of polarization and vignetting of the detector box. In addition, it was latter discovered that the nitrogen channel was, indeed, out of alignment.

The comparison of measured and modeled profiles, for both Rayleigh and Raman channels, has identified further areas which need to be analyzed and corrected in the future in order to improve the expected photon return model. These areas will be addressed in the next section.

6.3 Future Improvements to the Lidar System

Throughout the discussion of the comparison of measured and modeled data, it was shown that it is difficult to account for the effects of atmospheric transmission and depolarization on the detected signal. Methods to account for extinction are currently being worked on in order to extract the molecular profile from the detected signal. Also, the development of an instrument to track and measure the intensity of the light emitted from a star, would provide an estimation of the atmospheric transmission. Accounting

for extinction would better pin down the performance of the LAMP system. Vignetting and polarization remain constant when in a stable environment, and can be measured with the proper equipment. In order to improve the expected photon return model, further analysis of each of these parameters needs to be made.

Chapter 7

CONCLUSION

The performance of the Penn State LAMP lidar system has been analyzed by comparing measured LAMP data and expected photon returns computed by a model program. The calculations in the model were based on the lidar equation in Chapter 2. In order for the comparison to be valid, the environmental conditions and the efficiencies of the LAMP lidar at the time of measurement had to be incorporated into the model. Further analysis of the other parameters of the lidar equation was presented in order to account for any deviation of the measured data from the model calculations.

The two phenomena exploited by the LAMP system are Rayleigh scattering, which includes scattering at the Cabannes line and rotational Raman shifting to the sides of the Cabannes line, and Raman scattering, which includes both rotational and vibrational shifting from the central wavelength. Particle scattering, evident in the troposphere and lower stratosphere, was also seen in the measured data profiles. It caused deviations from the model predictions, making performance analysis difficult in those regions.

Transmission is based on the absorption and scattering properties of the molecules that make up the atmosphere. The LOWTRAN 7 atmospheric model was used to calculate the transmission of the detected wavelengths, 355 nm, 532 nm, 607 nm, and 660 nm, from the ground to 100 km. LOWTRAN 7 can not account for all of the variabilities of the atmospheric constituents that influence transmission through the atmosphere. Thus, it can not represent the conditions at the time of measurement with total accuracy.

Optical efficiencies for the transmitter, receiver, and detector subsystems were obtained with a Cary 5 spectrophotometer and data sheets provided by the manufacturers. The energy of the laser was measured pulse by pulse with an energy monitor calibrated with a Scientech calorimeter. The receiver probability factor, which accounts for vignetting in the near field of the telescope, was calculated using a simulation program for the LAMP classical Cassegrain telescope. These factors were tabulated and incorporated in the model calculations to give an expected maximum photon return for the atmospheric and instrument conditions at the time of measurement.

In all cases, as was expected, the measured data was below the expected photon return, except where large scattering aerosol layers existed. The differences from the model ranged from a factor of five to a factor of fifteen, and was due to a combination of vignetting and polarization losses in the detector system, extinction due to aerosols, and atmospheric depolarization.

Further studies to pin down the exact polarization orientation and vignetting of the detector box need to be made in order to improve the photon return compared to the model. The performance model can provide a good indicator as to when the lidar is in good operating condition.

REFERENCES

1. M. L. Chanin, A. Hauchecorne, "LIDAR studies of temperature and density using Rayleigh scattering," *MAP Handbook*, no. 13, 87 - 99, 1984.

2. L. B. Elterman, "The measurements of stratospheric density distribution with the search light technique, *J. Geophys. Res.*, 58, 519-530, 1953.

3. J. C. Farman, B. G. Gardner, and J. P. Shanklin," Large losses of total ozone in Antarctica Reveal seasonal ClOx/NOx interaction," *Nature*, vol. 315, pp. 207-210, 1988.

4. R. W. Fenn, S. A. Clough, W. O. Gallery, R. E. Good, F. X. Kneizys, J. D. Mill, L. S. Rothman, E. P. Shettle, F. E. Volz, "Optical and infrared properties 6 the atmosphere," *Handbook of Geophysics and the Space Environment*, 18-1 to 18-80, 1985.

5. J. Hansen, A. Lacis, R. Ruedy, and M. Sato, "Potential climate impact of the Mount Pinatubo eruption," *Geophysical Research Letters*, vol. 19, no. 2, pp. 215-218, 1992.

6. E. Hecht, *Optics*. Massachusetts: Addison-Wesley Publishing Company, 1987.

7. F. X. Kneizys, E.P. Shettle, L.W. Abreu, J. H. Chetwynd, G. P. Anderson, W. O. Gallery, J. E. A. Selby, S. A. Clough, "Users Guide to LOWTRAN 7," *AFGL-TR-88-0177*, Environmental Research Papers, no. 1010, Geophysics Laboratory, 1988.

8. T. H. Maiman, "Stimulated optical radiation in ruby," *Nature*, 187, pp. 493-494, 1960.

9. F. J. McClung and R. W. Hellwarth, "Giant optical pulsations from ruby," *J. Appl. Phys.*, 33, pp. 828-829, 1962.

10. R. M. Measures, *Laser remote sensing*. New York: John Wiley & Sons, 1984.

11. L. T. Metzger, C. S. Gardner, "Temperature determination from Rayleigh lidar," *EOSL rep. # 89-001*, University of Illinois, 1989.

12. J. H. Moore, C. C. Davis, M. A. Coplan, *Building scientific apparatus*, California: Addison-Wesley Publishing Company, 1989.

13. *Optics & Filters*, catalog vol 3, Connecticut: Oriel Corporation, 1990.

14. *Optics Guide 4*, California: Melles Griot, 1988.

15. C. R. Philbrick, D. B. Lysak, T. D. Stevens, P. A. T. Haris, and Y. -C. Rau, "Atmospheric Measurements using the LAMP lidar during the LADIMAS campaign," *Proceedings of the 16th International Laser Radar Conference*, NASA Conference publications, no. 3158 , pp. 651 to 654, 1992.

16. C. R. Philbrick, F. J. Schmidlin, K. U. Grossman, G. Lange, D. Offerman, K. D. Baker, D. Krankowsky, and U. von Zahn, "Density and temperature structure over northern Europe," *J. Atmos. Terr. Phys.*, vol. 47, pp. 159-172, 1985.

17. C. R. Philbrick, D. P. Sipler, B. E. Dix, G. Davidson, W. P. Moskowitz, C. Trowbride, R. Sluder, F. J. Schmidlin, L.D. Mendenhall, K. H. Bhavnani, and K. J. Hahn, "Measurements of the high latitude middle atmosphere properties using LIDAR," *AFGL-TR-87-0053, Environmental Research Papers*, no.976, Geophysics Laboratory, 129 pages, 1987.

18. C. R. Philbrick, D. P. Sipler, G. Davidson, and W. P. Moskowitz, "Remote sensing of structure properties in the middle atmosphere using lidar," *Proceedings of OSA Meeting on Laser and Optical Remote Sensing*, pp 120-123, 1987.

19. H. Rutten and M. van Venrooij, *Telescope optics: evaluation and design*. Virginia: Willmann-Bell, 1988.

20. A. L. Schawlow and C. H. Townes, "Infrared and optical masers," *Phys. Rev.*, 112, pp. 1940-1949, 1958.

21. T. D. Stevens, "An optical detection system for a Rayleigh/Raman lidar," MS Thesis, The Pennsylvania State University, 1992.

22. T. D. Stevens, P. A. T. Haris, Y. -C. Rau, C. R. Philbrick, "Latitudinal lidar mapping of stratospheric particle layers," accepted for publication in *Adv. in Spac. Res.*, 1993

23. L. L. Stowe, R. M. Carey, and P. P. Pellegrino, "Monitoring the Mt. Pinatubo aerosol layer with NOAA/11 AVHRR data," *Geophysical Research Letters*, vol. 19, no. 2, pp. 150-162, 1990.

24. U.S. Standard Atmosphere, 1976, National Oceanic and Atmospheric Administration, Washington, D.C., 1976.

25. S. L. Valley, Ed., "*Handbook of geophysics and space environments*," McGraw-Hill, New York, 1965.

26. U. von Zahn, R. Neuber, Thermal structure of the high latitude mesopause region in winter, *Contrib. Atmos. Phys.*, 60, pp. 294-304, 1987.

27. A. T. Young, "Rayleigh scattering," *Applied Optics*, vol. 20, no. 4, pp. 533-535, 1981.

Appendix

DISCRETE PULSE ENERGY MONITOR

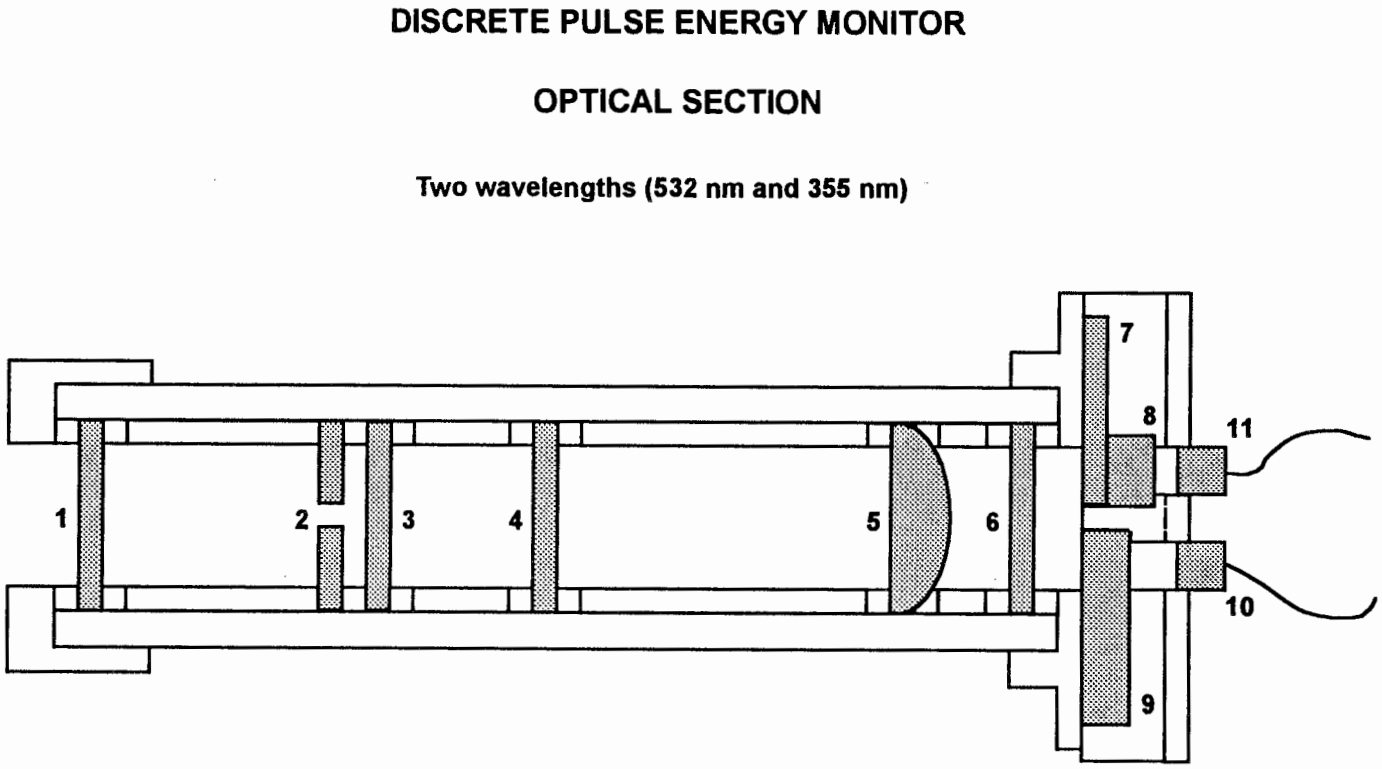

Figure 29. Schematic drawing of the discrete pulse energy monitor.

Key to Figure 29

1) Gray glass difusser, d = 25.4 mm.

2) Aperture, d= 25.4 mm, aperture d = 1.5875 mm.

3) Gray glass difusser, d = 25.4 mm.

4) Gray glass difusser, d = 25.4 mm.

5) Glass plano-convex lens, d = 25.4 mm, F = 50.8 mm.

6) Glass neutral density filter, d = 25.4 mm, ND = 3.0.

7) Glass neutral density filter, d = 25.4 mm, ND = 1.0.

8) 532 nm narrow band pass filter, d = 12.7 mm, transmits 50 % at 532 nm.

9) 355 nm narrow band pass filter, d = 25.4 mm, transmits 31.3% at 355 nm.

10) EG&G Photon Decices' HFD-1064 ultra-fast photodiode with amplifyer.

11) EG&G Photon Decices' HFD-1064 ultra-fast photodiode with amplifyer, 10% of 532 nm sensitivity at 355 nm.

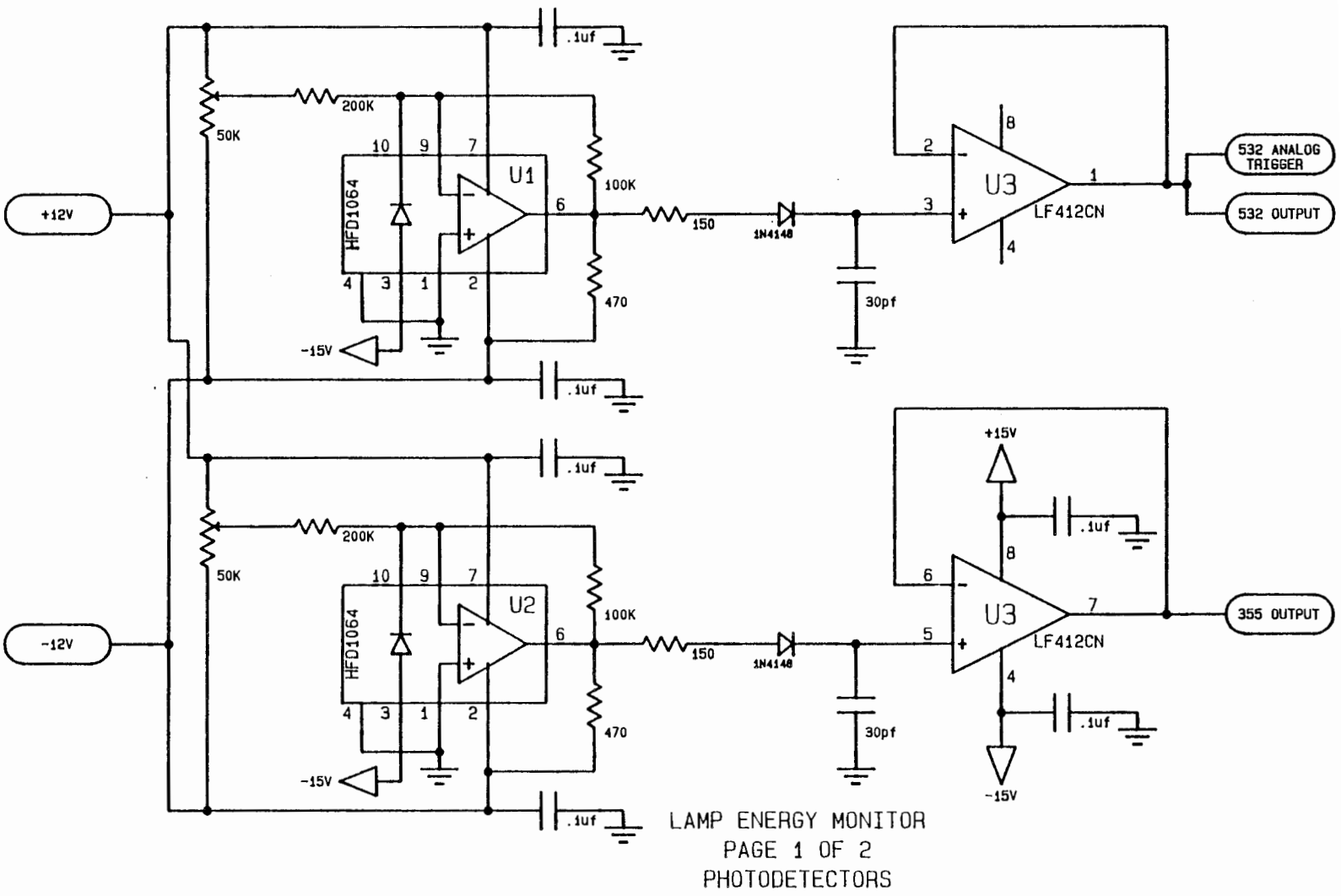

Figure 30. High speed photoelectric circuit diagram for the energy monitor.

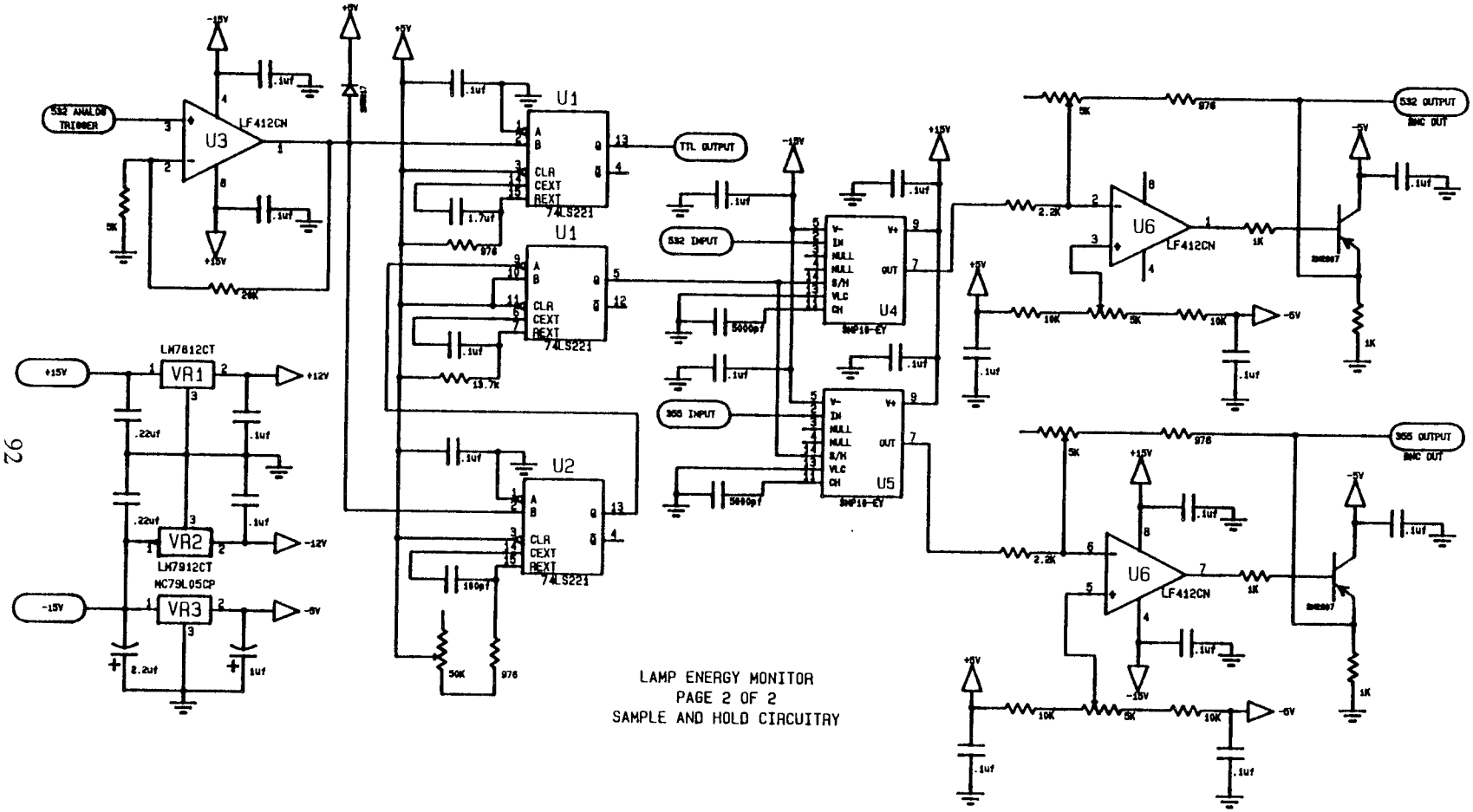

Figure 31. Sample and hold circuit diagram for the energy monitor.

“Latitude Variation of Middle Atmosphere Temperatures,” P. A. T. Haris, T. D. Stevens, S. Maruvada and C. R. Philbrick, **Adv. Space Res.**, 14, (9)83-(9)87, 1994.

LATITUDINAL VARIATION OF MIDDLE ATMOSPHERIC DENSITY AND TEMPERATURES

P.A.T. Haris, T.D. Stevens, S. Maruvada, C.R. Philbrick
The Pennsylvania State University, Applied Research Laboratory,
Communication and Space Sciences Laboratory
University Park, Pennsylvania, U.S.A.

ABSTRACT

Profiles of the latitudinal distribution of middle atmospheric density and temperature have been obtained from a ground based remote sensing instrument. A two color Rayleigh/Raman lidar, built at Penn State University, was part of the LADIMAS (Latitudinal Distribution of Middle Atmospheric Structure) campaign. The goal was to measure density, temperature, and trace constituents from the troposphere to the thermosphere on a global scale. Measurements were taken from 70° North to 65° South latitude during a three month period between September, 1991 and January 2, 1992. The data provides a unique opportunity to study the latitudinal variations of the mean temperature and the variability in the atmospheric structure. Comparisons of the atmospheric conditions to models, such as the CIRA atmospheric model, were made to study the deviations.

INTRODUCTION

During the past couple of decades, there has been an increasing interest in monitoring and studying the structure and dynamics of the middle atmosphere [1,2] using numerous techniques with varying accuracies and resolutions. Among the more common types are radiosonde balloons, rocket launched passive spheres and datasondes, satellites, and various remote sensing instruments. Each of these devices have two things in common: limited continuous data

gathering times, and high cost. In the early 1950s, Elterman experimented with a searchlight and telescope to show that optical detection and ranging was useful for measuring atmospheric structure and properties [3]. From that beginning, lidar was conceived, and with the development of the laser source, has grown into a most versatile atmospheric monitoring device [4].

In the past decade new developments, particularly in lasers, optical filters, detectors, and fast electronics, have improved the reliability, stability, and affordability of the basic lidar system. With high powered lasers and large telescopes, measurements of atmospheric constituents can be made from the ground to the lower thermosphere. Lidar is now capable of making continuous measurements at relatively low costs and with relative ease of operation [5].

Size reduction has allowed lidars to be installed in mobile units and transported to various locations. This gives lidar a distinct advantage over other techniques, such as rocket instruments which need a launch complex, use expendable hardware, and need numerous support personnel for telemetry recording, radar tracking, and rocket launching. A mobile lidar only needs two operators and electrical power. The Phillips laboratory in Massachusetts has had a mobile lidar since 1985 [6] which was a forerunner of the LAMP system. Mobile lidars have been installed in trailers, aircraft, ships, and soon on satellites. France has had a ship-board lidar system since 1989 which makes routine measurements at various locations on the Atlantic ocean [5].

A Rayleigh/Raman lidar system was constructed at Penn State University during 1990 - 1991. In July 1991, the lidar was installed in a standard shipping container, which was designed to serve as a field laboratory. This system was completed in the Fall of 1991 and shipped to the Andoya Rocket Range in Norway for testing in preparation for the LADIMAS campaign. This campaign marked the first time that a lidar system has made measurements over such a latitudinal range. Satellite measurements have mapped a latitudinal distribution of atmospheric temperatures

and densities, but with lower vertical resolution. Satellite measurements, as well as rocket measurements from several sites, have provided the data which are the basis for the latitudinal dependence of the CIRA Atmospheric model. It is the intention of this paper to present temperature and density profiles from the Penn State LAMP (Laser Atmospheric Measurement Program) lidar system and compare them to the CIRA: 1986 [7] and US Standard Atmospheric (USSA76) models [8]. Most measurements were taken on-board the German research vessel RV POLARSTERN. A description of the voyage and meteorological conditions, together with a description of the instrument and signal processing techniques, are presented.

DATA COLLECTION SITES

Data were collected at three locations: Andoya, Norway; Bremerhaven, Germany; and aboard the German research vessel RV Polarstern in transit from the Arctic to Antarctic oceans. The first part of the LADIMAS campaign, in late September and early October, was at the Andoya Rocket Range, Norway, during the METALS campaign, headed by U. von Zahn of the University of Bonn. Data were collected during several rocket launches so that comparisons could be made between the LAMP instrument and standard meteorological techniques. Efforts to collect data between Norway and Germany were hampered by stormy weather. During the stay in Bremerhaven, Germany, between October and early November, final adjustments were made to the system in preparation for the main part of the campaign aboard the RV Polarstern. The Polarstern is a German research vessel that was designed and built as an icebreaker to be the main resupply ship for research in Antarctica. While making its voyage each year or two, the Polarstern is a host to numerous scientific investigators. Figure 1 shows the path and data collection sites for our voyage from Bremerhaven to Puerto Madryn, Argentina. We obtained

data between 50 degrees North latitude and 65 degrees South latitude on 25 separate days, under all types of weather conditions.

INSTRUMENTATION

The Penn State LAMP lidar was designed as a Rayleigh/Raman system with the goal of measuring density and temperature from altitudes of 0.5 km to 80 km, and concentrations of gases, nitrogen and water vapor from the 0.5 km to 35 km and 5 km, respectively.

The instrument consists of five principal subsystems: transmitter, receiver, detector, data system, and safety system. Light is emitted from a Nd:YAG laser, at a pulse repetition rate of 20 Hz with 7 ns long pulses, providing approximately 250 mJ pulses in the ultraviolet (355 nm) and 600 mJ pulses in the visible (532 nm). The energy in each pulse is measured and recorded by the data system. The laser beam is expanded through a five power telescope and directed into the atmosphere on the axis of the receiving telescope. The receiver consists a 16" classical Cassegrain telescope with several beam steering components. The detector box utilizes a unique shuttering system and six separate detector channels to detect both high and low altitude data. The high altitude signal is shuttered over the first 10 km to prevent saturation of photon counting PMT's. A high speed data acquisition system allows 15 m resolution in the lower altitudes and 75 m resolution in the higher altitudes. The signal is counted and averaged for one minute (1200 laser shots) by a CAMAC unit and stored on an optical disk.

SIGNAL PROCESSING

In order to average out any small scale wave structures, the data was height reduced to 1 km and integrated from 1 to 4.5 hours, depending on the meteorological conditions at the time

of measurement. Long integrations reduce the superposition of waves which could cause larger temperature fluctuations and deviations from the mean temperature. Background was eliminated by subtracting the averaged tail end of the signal, where the signal was of insignificant value, and fitting the tail end of the signal to the CIRA model [1]. The raw data was then processed using a Hanning filter with a window size that increased with increasing altitude. The window has a minimum size of 2 km at 20 km altitude and a maximum size of 7.8 km at 70 km altitude.

Temperature calculations from Rayleigh lidar data can be achieved by integrating down relative density profiles using the hydrostatic equation and ideal gas law. This process assumes that there are no contributions from aerosols. In the past, the lower limit for aerosol free signals was near 20 km. After the El Chichon volcano erupted, the aerosol contamination of the molecular signal rose as high as 38 km. The aerosol effect decreased after a period of natural settling but was then lifted back up to 34 - 40 km by the eruption of Mount Pinatubo. The hydrostatic assumption is not entirely accurate when a strong localized turbulent layer is present. However, large spatial and temporal integrations reduce these effects making it a good approximation [2]. The hydrostatic and ideal gas law are,

$$dP = -\rho g dz, \tag{1}$$

$$P(z) = \frac{\rho(z)\, T(z)\, R}{M}, \tag{2}$$

were R is the gas constant for dry air, $\rho(z)$ is the density at altitude z, g is the acceleration of gravity, P(z) is the pressure at altitude z, and M is the mean molecular weight of the atmosphere. Combining these two equations and solving for temperature [9],

$$T(z_1) = \frac{T(z_2)\,\rho(z_2)}{\rho(z_1)} + \frac{M}{R}\int_{z_1}^{z_2} \frac{g(z)\,\rho(z)}{\rho(z_1)}\,dz\,. \qquad (3)$$

All that is needed to start the integration is a starting temperature which can be found in atmospheric models.

ERROR ANALYSIS

The three main sources of deviations from the mean density and temperature that will be addressed in this paper are background error, atmospheric dynamics, and assumed initial starting temperature.

Background Error: It is extremely important to subtract the proper background from the raw signal in order to obtain accurate temperature measurements [10]. Due to the shutter wheel configuration, there were only a few data points on the top end of the signal for which an average background could be calculated. Fluctuations in this value made it difficult to pin down an exact value [11]. The shutter wheel is to be modified for future measurements. Background errors, N_B, can alter the temperature, $\Delta T(z_1)$, by the equation [10],

$$\Delta T(z_1) \approx \frac{z_2}{H}\,\frac{T(z_1)}{N(z_1)}\,\Delta N_B\,. \qquad (4)$$

As the photon count approaches closer to the possible background error, larger temperature errors are incurred. On the other hand, the larger photon counts in the lower altitudes are not effected as much. Figure 2 shows a series of possible effects on the temperature from subtracting incorrect background from the US Standard Atmospheric model density. At 45 km a subtraction of 1 count means a relative density error of 0.1 %, while a subtraction of 7 counts makes a relative density error of 1.2 %.

Atmospheric Dynamics: It is difficult to draw comparisons to monthly and latitudinal mean temperatures with only a few hours of measured data. Significant fluctuations can be seen in 5 and 30 minute data samples from the effects of gravity wave propagation [4]. However, a few hours will smooth out most gravity wave components other than atmospheric tides. Since most of the measurements were limited to nighttime, the tidal components are probably not detectable. Further attempts at eliminating these fluctuations were achieved by reducing height resolution and by smoothing over large time and altitude intervals, in order to determine the mean properties for the model comparisons.

Starting Temperature: An inaccurate starting temperature for the integration can cause temperature errors throughout a measured profile. Figure 3 shows calculated temperature profiles, from the density of the US Standard Atmospheric model, starting with an initial incorrect temperature at 70 km. The deviation from the correct temperature, between 35 km and 70 km, can be significant. By selecting the cutoff end of the signal at a point where it matches closely with the CIRA model, these significant errors can be minimized. On average only a few kilometers of signal were sacrificed in order to gain greater temperature accuracies. This is clearly seen in Figure 4, where the signal was tied to 5% density error (62 km) and 2.5% density error (57 km). By starting the temperature integration at a lower density error, less temperature error is propagated down the curve.

OBSERVATIONS

During the METALS campaign at the Andoya Rocket Range, the LAMP lidar obtained data together with meteorological rockets. One of these comparisons is shown in Figure 5. The lidar data was integrated over 30 minutes and height reduced to 150 meters in order to closely

match the rocket resolution. Both the 355 nm and 532 nm data channels follow the rocket measurements closely. The error bars signify only the statistical error due to the number of photon counts.

Figures 6, 7, and 8, show two color data from the LAMP lidar during the LADIMAS campaign. The solid lines follows the CIRA model. Figure 6 demonstrates close correlation of the LAMP data to the CIRA model. Temperature is extended down to 25 km, since the Pinatubo dust layer was not very prominent above the lower stratosphere in the high latitude regions. Increases in wave activity, shown in both Figures 7 and 8, cause noticeable deviations from the CIRA model.

Figure 9 provides a summary of density ratios and temperatures for the entire LADIMAS campaign over several height intervals. The solid lines are the CIRA model ratio, while the circles are the measured average signal ratio. Data from the LAMP lidar was selected at 10° latitude, since the CIRA model only gives temperature and pressure data at 10° latitude intervals. The density ratio plots were obtained by forming the ratio of the CIRA model and the LAMP signal to the USSA76 model. The ratios to the USSA76 model provide information about how well the CIRA model and the present measurements agree in distribution over latitude and month. At 35 km altitude, between 40° S and the equator, the Pinatubo aerosols contaminate the signal and thus have been removed from the plot. Above 40 km there are no effects from the stratospheric aerosol layer. At 60 km there are a few missing points where the data did not achieve the limit of 4% statistical error. This is due to fluctuations in low altitude atmospheric transmission, caused mainly by heavy cloud coverage. The lines in Figure 9 are from the CIRA model. Since the LAMP data covers a four month period, seasonal changes in temperature and density are the main cause for the structure of the CIRA model over the latitudinal range of

Figure 9. We have found that the density and temperature, measured by the LAMP lidar, follow the CIRA model closely in these altitude regions.

CONCLUSIONS

The LAMP Lidar provided an enormous data base, which covers 70° N to 65° S latitude. There was a unique opportunity to compare our lidar results with established models, such as CIRA, which encompass the range of our of data. We have found, in this preliminary analysis, that there is a high degree of correlation between our temperatures and densities and the CIRA temperatures and densities.

The investigation has shown the impact of careful processing of data, which is absolutely necessary when analyzing Rayleigh data for density and temperature. Small errors in the density gradient will lead to very large errors in the temperature calculation. Great care must be taken, therefore, when subtracting the background, since so few signal counts exist at the higher altitudes.

ACKNOWLEDGMENTS

We would like to express our appreciation for support from NSF, the U.S. Navy's Environmental Systems Program Office, and the Pennsylvania State University's Applied Research Laboratory and College of Engineering. Participation in the LADIMAS campaign was made possible by the invitation of the Alfred-Wegener-Institute. Appreciation to several colleagues, particularly Professors U. von Zahn and D.Offermann, is gratefully acknowledged. The contributions made by Dr. D. Lysak, Yi-Chung Rau, and D.E. Upshaw are also greatly appreciated.

REFERENCES

1. M. L. Chanin, A. Hauchecorne, "LIDAR studies of temperature and density using Rayleigh Scattering," *MAP Handbook*, No. 13, 87 - 99, 1984.

2. C. R. Philbrick, "Measurements of structural features in profiles of mesospheric density," *MAP Handbook*, vol. 2, pp. 333 - 340, 1981.

3. L. B. Elterman, "The measurement of stratospheric density distribution with the search light technique," *J. Geophys. Res.*, 58, 519-530, 1953.

4. M. L. Chanin, A. Hauchecorne, "LIDAR observations of gravity and tidal waves in the middle atmosphere," *J. Geophys. Res.*, 86, 9715-9721, 1981.

5. A. Hauchecorne, M. L. Chanin, P. Keckhut, D. Nedeljkovic, "LIDAR monitoring of the temperature in the middle and lower atmosphere," *Appl. Phys.*, B 55, 29-34,1992.

6. C. R. Philbrick, D.P. Sipler, B. E. Dix, G. Davidson, W. P. Moskowitz, C. Trowbridge, R. Sluder, F. J. Schmidlin, L. D. Mendenhall, K. H. Bhavnani, K. J. Hahn, "Measurements of the high latitude middle atmosphere dynamic structure using lidar," *AFGL-TR-87-0053*, Environmental Research Papers, # 967, Geophysics Laboratory, 1987

7. COSPAR International Reference Atmosphere: 1986, Part II Middle Atmosphere Models, edited by D. Rees, J. J Barnett, K. Labitzke, Pergamon Press, Oxford,1990.

8. U.S. Standard Atmosphere, 1976, National Oceanic and Atmospheric Administration, 1976

9. C. R. Philbrick, F. J. Schmidlin, K. U. Grossmann, G. Lange, D. Offermann, K. D. Baker, D. Krankowsky, U. von Zahn, "Density and temperature structure over northern Europe," *Journal of Atmospheric and Terrestrial Physics*, vol. 47, No. 1 - 3, pp. 159 - 172, 1985.

10. L. T. Metzger, C. S. Gardner, "Temperature determination from a rayleigh lidar," EOSL rep. #89-001, University of Illinois, 1989.

11. C. A. Hostetler, C. S. Gardner, "Rayleigh LIDAR signal processing techniques for Studies of stratospheric temperature structure and dynamics," *EOSL rep. # 90-003*, University of Illinois, 1990.

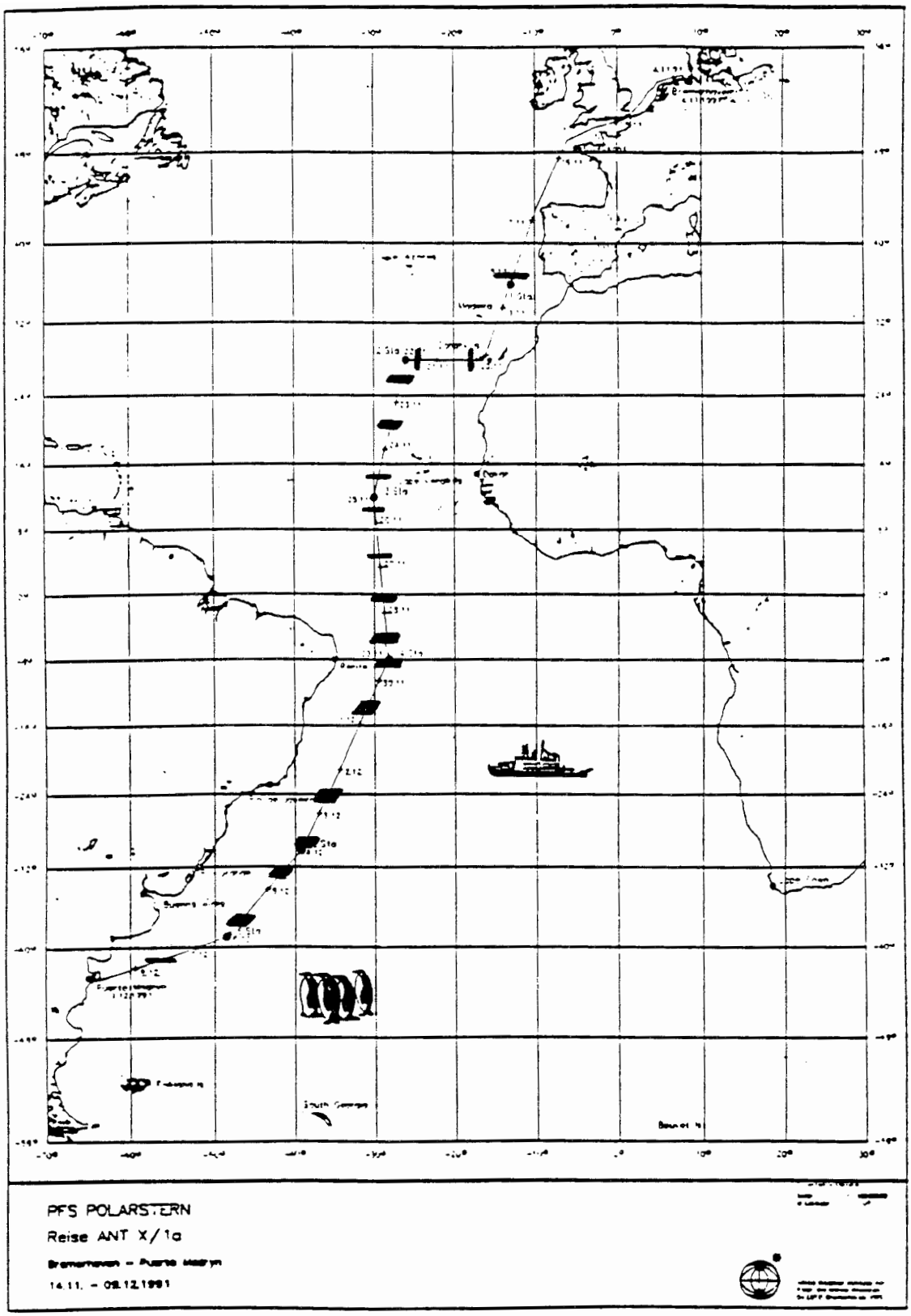

Figure 1. Map of the first leg of the RV POLARSTERN Antarctic voyage. The horizontal lines mark the position and duration of lidar measurements.

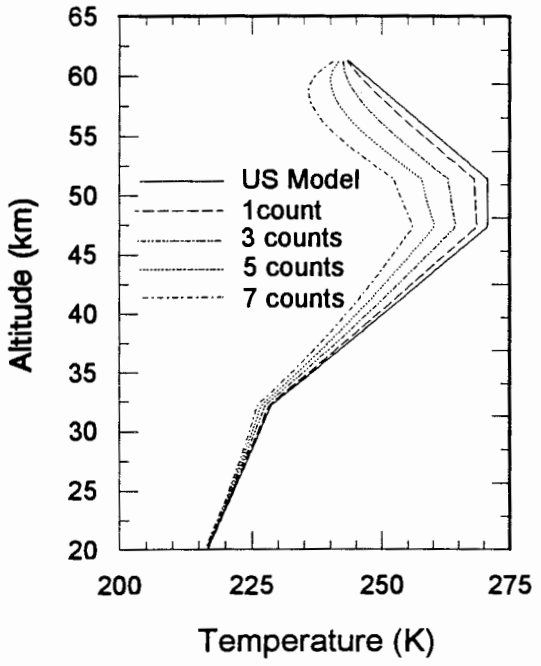

Figure 2. Temperature errors caused by background subtraction errors.

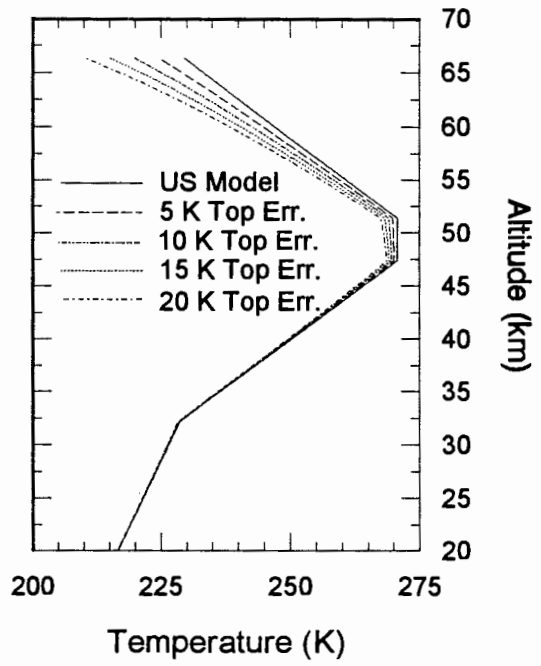

Figure 3. Temperature errors caused by an incorrect initial integration temperature.

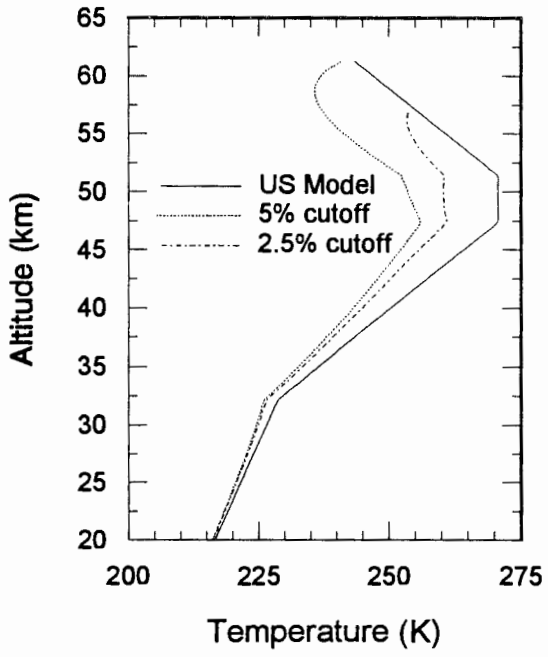

Figure 4. Propagation of background error in the temperature profile for two cutoff statistical errors.

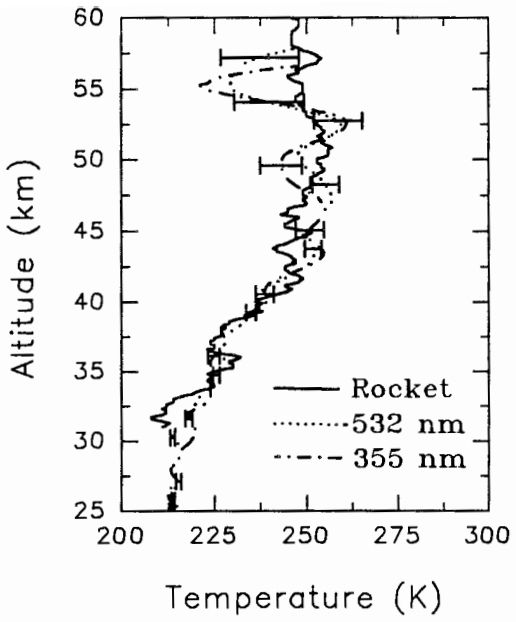

Figure 5. Comparison of Rocket and LAMP lidar data using 532 and 355 nm wavelengths. 11/04/91 0039 UT. 30 minute average.

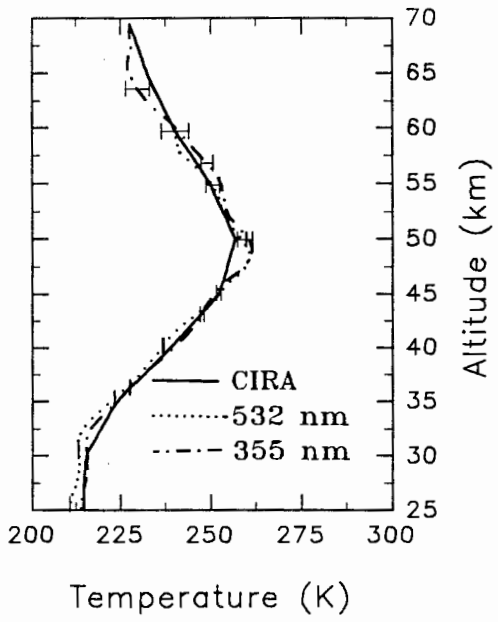

Figure 6. Comparison between CIRA: 1986 Atm. model and LAMP lidar data measured on 11/10/91 at 1712 - 1817 UT. 60 minute average.

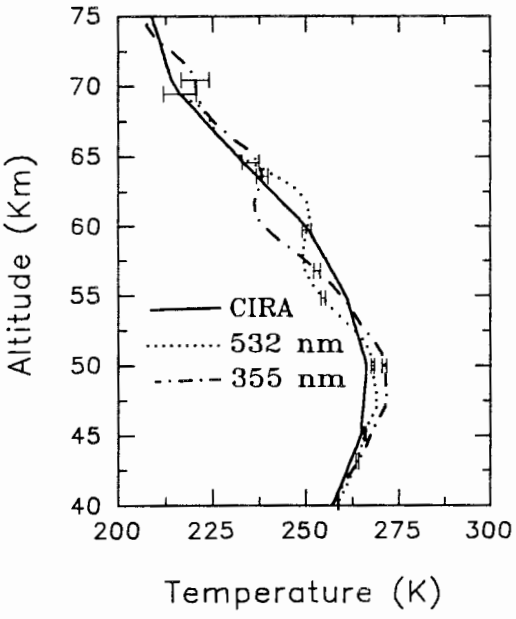

Figure 7. Comparison between CIRA: 1986 Atm. model and LAMP lidar data measured on 12/01/91 at 0026 - 0650 UT. 270 minute average.

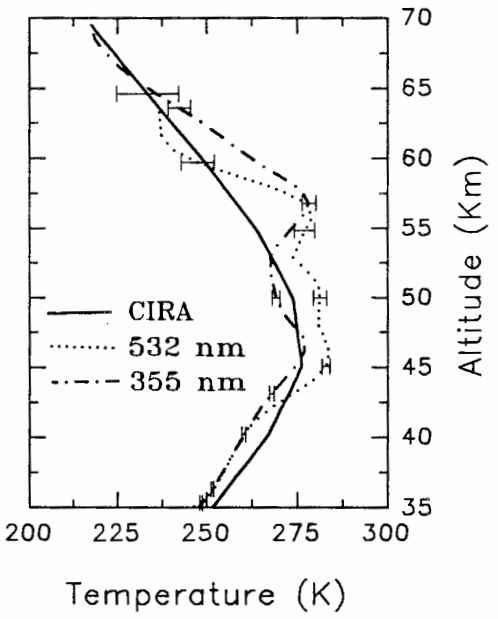

Figure 8. Comparison between CIRA: 1986 Atm. model and LAMP lidar data measured on 12/06/91 at 0455 - 0632 UT. 90 minute average.

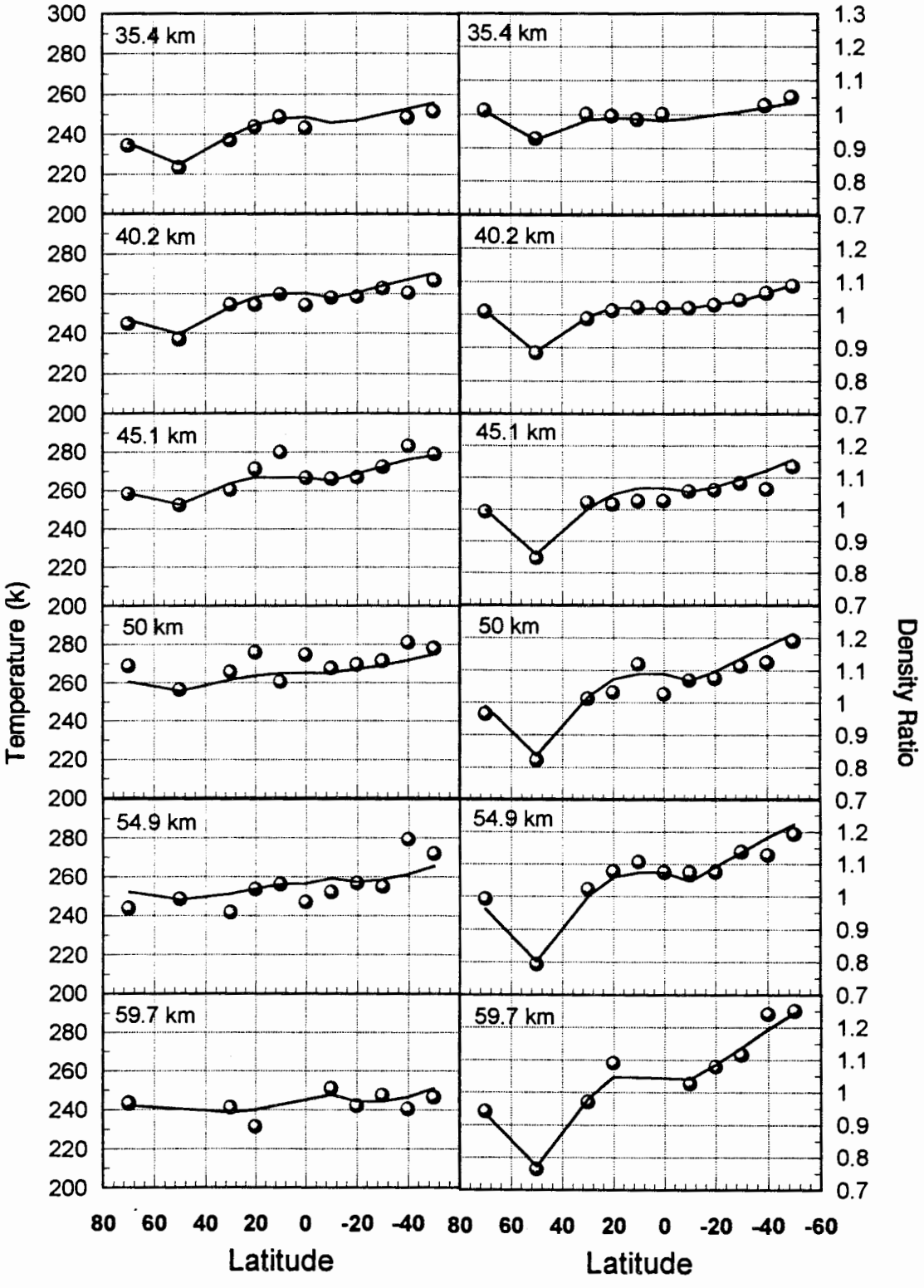

Figure 9. Temperature and density ratios for both LAMP data and the CIRA model as a function of latitude, season, and altitude.